Draft version August 24, 2022
Typeset using LaTeX **twocolumn** style in AASTeX63

Indication of a Local Source of Ultra-High-Energy Cosmic Rays in the Northern Hemisphere

Pavlo Plotko [1], Arjen van Vliet [1,2], Xavier Rodrigues [1] and Walter Winter [1]

[1] *Deutsches Elektronen-Synchrotron DESY, Platanenallee 6, 15738 Zeuthen, Germany*
[2] *Department of Physics, Khalifa University, P.O. Box 127788, Abu Dhabi, United Arab Emirates*

ABSTRACT

The Pierre Auger Observatory (PAO) and Telescope Array (TA) collaborations report significant differences in the observed energy spectra of Ultra-High-Energy Cosmic Rays (UHECRs) above 30 EeV. In this work, we present a joint fit of TA and PAO data using the rigidity-dependent maximal energy model, and including full marginalization over all relevant parameters. We show that the presence of a local astrophysical source in the Northern Hemisphere, which is only visible by the TA experiment, can reconcile PAO and TA measurements up to the highest energies. We demonstrate that the presence of that local source is favored at the 5.6σ level compared to the scenario where both experiments observe the same isotropic UHECR flux. We also quantify that the astrophysical explanation can describe the current data better than a scenario where the differences in the observations are explained by experimental systematics (i.e., energy-dependent shifts). Having tested different mass compositions emitted from the local source, we conclude that the data are best described by a source lying at a distance of about 14 Mpc that emits cosmic rays dominated by the silicon mass group; we also discuss possible source candidates.

Keywords: astroparticle physics — cosmic rays — neutrinos — methods: numerical

1. INTRODUCTION

Ultra-high-energy cosmic rays (UHECRs) are the most energetic particles ever detected. These atomic nuclei with energies above 10^{18} eV are measured with increasing precision by the Pierre Auger Observatory (henceforth PAO, Aab et al. 2015), located in Argentina, and the Telescope Array (TA, Abu-Zayyad et al. 2013; Tokuno et al. 2012), located in the state of Utah, USA. Both PAO and TA employ a hybrid detection technique to detect the extensive air showers triggered in the atmosphere by the UHECRs: A surface detector array measures the charged secondaries that reach the ground level, while fluorescence detector stations measure the development of the air showers in the atmosphere. Located in the Southern Hemisphere, PAO observes the sky below a declination of 24.8° (Aab et al. 2020), while TA, located in the Northern Hemisphere, observes the sky above -16.0° (Ivanov 2019). There are therefore large portions of the Northern and Southern Hemispheres that are observed exclusively by TA and PAO, respectively, but there is also a common declination band, $-16.0° < \delta < 24.8°$, where the sky is observed by both experiments.

As quantified recently by a spectrum working group from PAO and TA (Ivanov 2017; Deligny 2019; Tsunesada et al. 2021), there are differences in the energy spectrum of the UHECRs as measured by both experiments, as shown in Fig. 1, adopted from that report. In the left plot, we see that using the energy scales native to both experiments there is a difference in the overall flux normalization, as well as the spectral shape at energies above $10^{19.5}$ eV, or about 30 EeV. Although Fig. 1 shows full-sky data, discrepancies are also present in the common declination band, albeit less significantly due to higher statistical uncertainties.

The total systematic uncertainty in the energy scale of PAO is estimated at 14% (Aab et al. 2020), while for TA it is 21% (Ivanov 2019). Shifting the energy scale of the experiments within these uncertainty ranges leads to a change in both the shape and normalization of the UHECR spectra, since they are plotted here as $E^3J(E)$. As shown by Deligny (2019), shifting the energy scales of the experiments by a constant value can mitigate the spectral differences below 30 EeV, as we can see in the right plot of Fig. 1. However, above that energy the spectra become again discrepant, with TA data showing an excess in flux compared to PAO.

For this discrepancy to be explained solely by systematic effects, energy-dependent shifts must be introduced in the energy scales of both experiments. Tsunesada et al. (2021) have recently quantified the expressions for

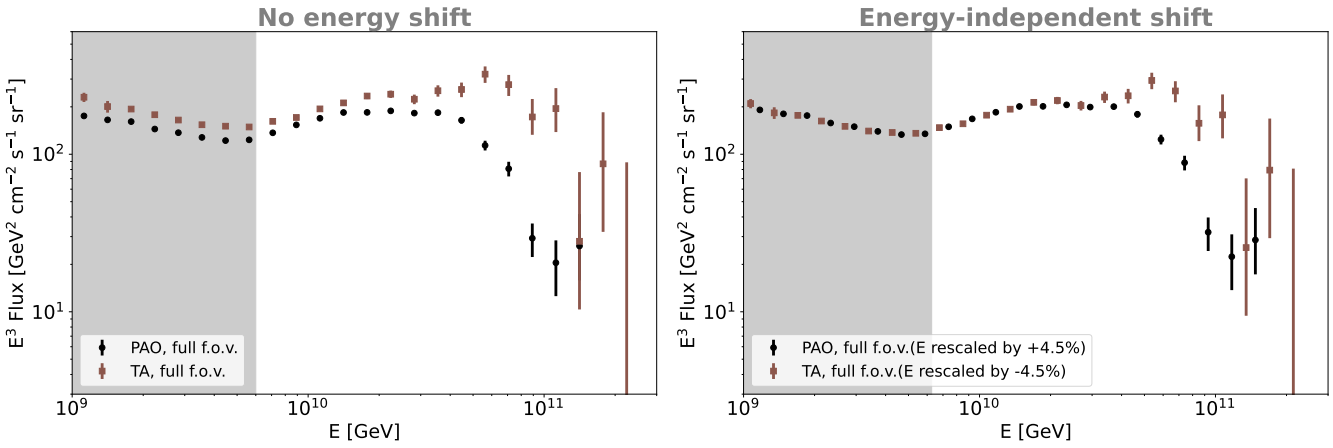

Figure 1. Energy spectrum of the UHECRs as measured by PAO (black) and TA (brown) in the full fields of view (f.o.v.) of each observatory. In the left plot, we see the data in the native energy scale of either experiment. In the right plot, those energy scales have been shifted by the amounts specified in the legend, which are within the uncertainty range given by the experiment systematics. With this constant energy shift, the spectra are compatible at energies below 30 EeV. Figure adapted from Tsunesada et al. (2021).

these shifts that lead to the best agreement between the data sets in the common declination band. At the same time, while the PAO spectrum is independent of declination, the TA spectrum seems to present different spectral features when considering events from the Northern Hemisphere compared to the common declination band (see also Abbasi et al. (2018a)). That means that the same energy-dependent shift in principle may not be sufficient to explain the difference in the entire sky (Ivanov 2017; Deligny 2019). This suggests an astrophysical origin of this discrepancy, namely a local source whose flux is observed by TA at the highest energies.

The existence of a nearby UHECR source or group of sources is also supported by previous analyses on the arrival directions of the TA cosmic rays. For example, using five years of data, Abbasi et al. (2014) reported an intermediate-scale anisotropy at 5.1σ Li-Ma significance in the arrival directions of UHECRs above 57 EeV. More recently, an update on that analysis with twice the exposure time has revealed that this hotspot is now significant at the 3.3σ level (Kim et al. 2021). Additionally, TA has also confirmed a new excess of events with energies above 25 EeV from a different direction (Abbasi et al. 2021a).

In this study, we investigate the hypothesis that a local source in the Northern Hemisphere is at least partially responsible for the discrepancy between the PAO and TA spectra. Using a cutting-edge numerical model, we simulate the propagation of UHECRs from a hypothetical local source observed only by TA, as well as an isotropically distributed population of sources observed by both experiments. We then perform a joint fit of the results to both TA and PAO data, considering both spectrum and composition observables and the relevant multi-parameter correlations. We then use the best-fit results to constrain the source properties.

The paper is structured as follows: in Sec. 2 we briefly describe the numerical method and specify the fitting procedure used to constrain the model parameters. In Sec. 3 we report the results of the fit and discuss their interpretation. In Sec. 4 we summarize our conclusions.

2. METHODS

2.1. *Source parametrization*

We first simulate the UHECR emission from an isotropically distributed continuous source population (*iso*). The sources are considered to have an emissivity in cosmic rays $\mathcal{L}_{\rm CR}^{\rm iso}$, defined as the emitted cosmic-ray luminosity per cosmic volume, and obtained by integrating above $E > 10^9$ GeV. Each emitted isotope of mass A contributes a fraction f_A of that emissivity. The set of all f_A values defines the emitted composition, which we assume to also be the same for all sources. The contribution of the isotropic source population to the observed flux spectrum of each element A, $J_A^{\rm iso}$, can then be written as (Heinze et al. 2019; Aab et al. 2017; Batista et al. 2019):

$$J_A^{\rm iso}(E) \;=\; J_0^{\rm iso}\; f_A\, f_{\rm cut}(E)\; n(z,m) \left(\frac{E}{10^9\ {\rm GeV}}\right)^{-\gamma^{\rm iso}}, \tag{1}$$

where $n \sim (1+z)^{m^{\rm iso}}$ is the cosmological source density (the index $m^{\rm iso}$ characterizes the evolution of the source density with redshift z), $\gamma^{\rm iso}$ is the spectral index of the emitted cosmic rays, $J_0^{\rm iso}$ is the normalization of

the spectra that corresponds to the total emissivity, and the factor $f_{\rm cut}$ introduces an exponential cutoff at the energy corresponding to the maximum rigidity $R^{\rm iso}_{\rm max} = E_{\rm max}/Z_{\rm A}$:

$$f_{\rm cut}(E) = \begin{cases} 1 & , E < Z_{\rm A} R^{\rm iso}_{\rm max} \\ \exp\left(1 - \frac{E}{Z_{\rm A} R^{\rm iso}_{\rm max}}\right) & , E > Z_{\rm A} R^{\rm iso}_{\rm max}, \end{cases} \quad (2)$$

The maximum rigidity $R^{\rm iso}_{\rm max}$ of all emitted isotopes is the same, as is typical of sastrophysical sources optically thin to nuclear disintegration (Kotera et al. 2015; Rodrigues et al. 2018; Biehl et al. 2018).

Regarding the injection composition (i.e. the chemical composition of the cosmic rays as they are emitted by the sources), we consider a combination of five elements, each representative of a distinct mass group up to iron-56: ^{1}H, ^{4}He, ^{14}N, ^{28}Si and ^{56}Fe. In terms of the propagation simulation, we start with a combination of these five isotopes at the source (whose fractions are given by f_A as discussed above). As they interact with the cosmic photon backgrounds, they then produce nuclear cascades of hundreds of secondary isotopes with intermediate masses, all of which are taken into account.

We also assume the existence of a single local source in the Northern Hemisphere, which can be observed by TA but not by PAO. For simplicity, we explore scenarios where the local source emits only one of the five mass groups given above, which is done by propagating the respective representative isotope. Therefore, the emission from this source can be fully characterized by a maximum rigidity $R^{\rm local}_{\rm max}$, power-law index $\gamma^{\rm local}$, emission luminosity $L^{\rm local}_{\rm CR}$, and one emitted cosmic-ray mass group. These parameters will be varied independently from those describing the isotropic source population. Finally, the comoving distance to the local source[1] will affect the UHECR spectrum observed at Earth, similar to the evolution parameter $m^{\rm iso}$ in the case of the isotropic source population.

Overall, the isotropic source population can be fully characterized by eight parameters $\boldsymbol{\lambda}^{\rm iso}$, and the local source by five parameters $\boldsymbol{\lambda}^{\rm local}$:

$$\begin{aligned} \boldsymbol{\lambda}^{\rm iso} &= (\gamma^{\rm iso}, R^{\rm iso}_{\rm max}, m^{\rm iso}, \mathcal{L}^{\rm iso}_{\rm CR}, \boldsymbol{f}^{\rm iso}_{\rm A}), \\ \boldsymbol{\lambda}^{\rm local} &= \left(\gamma^{\rm local}, R^{\rm local}_{\rm max}, D^{\rm local}, L^{\rm local}, A^{\rm local}\right). \end{aligned} \quad (3)$$

2.2. *Propagation model*

[1] We will generally refer to the comoving distance to the local source, while keeping in mind that the cosmic rays generally travel a longer distance due to magnetic field deflections, which cannot be included in a one-dimensional simulation. This distinction becomes more relevant the larger the value of $D^{\rm local}$.

Once we characterize the emitted UHECR spectra from the isotropic sources and the local source with two sets of parameters $\boldsymbol{\lambda}^{\rm iso}$ and $\boldsymbol{\lambda}^{\rm local}$ (Eq. 3), we then inject those cosmic rays into a numerical simulation to calculate their interactions as they propagate toward Earth. For this, we use the open-source software PriNCe (Heinze et al. 2019), which numerically solves the transport equations of the cosmic-ray spectra. We use Talys (Koning et al. 2007) as the nuclear interaction model, and we adopt the Extragalactic Background Light (EBL) model by Gilmore et al. (2012).

In the case of the isotropic source population, we consider the emission from a continuous distribution of sources up to $z = 1$, since a source at any higher redshift will lie outside the cosmic-ray horizon for the energy range we focus on. In each simulation, we assume a certain value of the evolution parameter $m^{\rm iso}$, which defines the strength of the cosmological evolution of the isotropic population, as defined in Eq. (1).

We then add the contribution from the local source. In the PriNCe framework, a single source lying at a comoving distance $D^{\rm local}$ is equivalent to a source population whose evolution is described by a delta function, $n = \delta(D = D^{\rm local})$. Because the isotropic source distribution and the local source are independent, we simulate the propagation of the two separately. We then add the respective contributions at Earth to obtain the prediction for the total flux observed by TA, while for PAO observables only the contribution from the isotropic source population is considered.

After simulating the cosmic ray propagation according to the above procedure, we obtain the energy spectrum for each individual isotope at the top of the atmosphere, as well as values of $\langle \ln A \rangle$ and $\sigma^2_{\ln A}$ for each energy of the numerical grid. We then compute the mean of the distribution of the depth of the shower maximum, $\langle X_{\rm max} \rangle$, as well as its second moment, $\sigma(X_{\rm max})$, following the procedure by Heinze et al. (2019). Throughout this work, we will discuss the results for three air shower models separately: Sibyll 2.3c (Riehn et al. 2016), Epos-LHC (Pierog et al. 2015), and QGSJET-II-04 (Ostapchenko 2011). These predictions will then be compared with data from both the TA and PAO experiments, resulting in a joint fit.

2.3. *Joint fit of PAO and TA data*

We aim at describing the spectrum and composition of UHECRs above $E_{\rm min} = 6 \times 10^9$ GeV, originating from the entire field of view of TA and PAO. The data from PAO consists of spectrum measurements distributed over fourteen energy bins (Verzi 2019), nine data points describing $\langle X_{\rm max} \rangle$, and nine more for

$\sigma(X_{\rm max})$ (Yushkov 2019). The TA spectrum above our threshold is described by fifteen data points and one upper limit (Ivanov 2019), while the data on $\langle X_{\rm max}\rangle$ and $\sigma(X_{\rm max})$ consist of five data points each[2] (Abbasi et al. 2018b).

Regarding the composition observables, i.e. $\langle X_{\rm max}\rangle$ and $\sigma(X_{\rm max})$, we adopt the values published by the two experiments independently. As argued by de Souza (2017), a detailed comparison should take into account the different detector acceptances and resolutions, as well as the differences between the analysis techniques of the two groups. However, the tools and data for such detailed treatment have not thus far been disclosed. Furthermore, as shown in Sec. 3 and previously by Heinze et al. (2019), the three air shower models considered in this work lead to different predictions on the observed composition, which introduces an element of uncertainty that surpasses the uncertainty from these more detailed effects. We, therefore, compare the composition data at face value and leave a more precise analysis for a future work.

As described in Sec. 2.1, we hypothesize that these data are explained by an isotropic source population, characterized by eight parameters $\boldsymbol{\lambda}^{\rm iso}$, and a local source in the Northern Hemisphere, characterized by five parameters $\boldsymbol{\lambda}^{\rm local}$. To account for the systematic uncertainties of TA and PAO, we further introduce six nuisance parameters $\boldsymbol{\delta}$: $\delta_E^{\rm TA}$ and $\delta_E^{\rm PAO}$ characterize the uncertainties in the energy scales of the TA and PAO spectra, respectively (see Sec. 1). Furthermore, we have $\delta^{\rm TA}_{\langle X_{\rm max}\rangle}$ and $\delta^{\rm PAO}_{\langle X_{\rm max}\rangle}$, which define systematic shifts in $\langle X_{\rm max}\rangle$, and $\delta^{\rm PAO}_{\sigma(X_{\rm max})}$ and $\delta^{\rm TA}_{\sigma(X_{\rm max})}$, which define a systematic shift in $\sigma(X_{\rm max})$.

As discussed in Sec. 1, different functional forms have been proposed for the energy shifts $\delta_E^{\rm PAO}$and $\delta_E^{\rm TA}$. In the main part of this work we will limit ourselves to the case of energy-independent energy shifts, $\delta_E^{\rm PAO}$= const. and $\delta_E^{\rm TA}$= const., given as a percentage of each energy bin. We explore values of δ within the uncertainty range of either experiment ($\pm14\%$ for $\delta_E^{\rm PAO}$ and $\pm21\%$ for $\delta_E^{\rm TA}$ as described in Sec. 1). In App. A we will consider, additionally, the more complex scenario where the experiments have energy-dependent systematic energy shifts, and we show that even in that scenario a local source is still compatible with the data. Interestingly, however, our baseline model, i.e. energy-independent systematics and a local source in the Northern Sky, actually provides the best joint fit to the data of all the scenarios tested, including those with energy-dependent systematics.

Regarding the composition observables, there is no precedent in the literature for the treatment of their systematic shifts in a joint fit, because to date no such joint fit has been performed. We assume that $\delta_{X_{\rm max}}$ is given as a percentage of the systematic uncertainty of each $X_{\rm max}$ data point, and likewise $\delta_{\sigma(X_{\rm max})}$ as a percentage of each $\sigma(X_{\rm max})$ data point. We treat the $\boldsymbol{\delta}$ variables as nuisance parameters, independent from each other and from the source parameters $\boldsymbol{\lambda}^{\rm iso}$ and $\boldsymbol{\lambda}^{\rm local}$. We search the range $\pm100\%$, which represents the boundaries of the systematic uncertainties carried by the data from either experiment. Like for the energy shifts, we consider only energy-independent values of $\delta_{X_{\rm max}}$ = const. and $\delta_{\sigma(X_{\rm max})}$ = const. in the main part of this text, while in App. A that condition is relaxed.

The goodness of fit relative to the PAO and TA data is calculated by means of a χ^2 test:

$$\begin{aligned}\chi^2_{\rm PAO} &= \chi^2_{\rm PAO}(\boldsymbol{\lambda}^{\rm iso},\, \delta_E^{\rm PAO},\, \delta^{\rm PAO}_{\langle X_{\rm max}\rangle},\, \delta^{\rm PAO}_{\sigma(X_{\rm max})}).\\ \chi^2_{\rm TA} &= \chi^2_{\rm TA}\ (\boldsymbol{\lambda}^{\rm iso},\, \boldsymbol{\lambda}^{\rm local},\, \delta_E^{\rm TA}\ ,\, \delta^{\rm TA}_{\langle X_{\rm max}\rangle},\, \delta^{\rm TA}_{\sigma(X_{\rm max})}),\end{aligned} \tag{4}$$

where we assume that the isotropic source distribution characterized by $\boldsymbol{\lambda}^{\rm iso}$ is observed by both experiments.

Finally, to compute the goodness of the joint fit, we combine the χ^2 values from both experiments with the systematic uncertainties:[3]

$$\begin{aligned}\chi^2_{\rm global}(\boldsymbol{\lambda}^{\rm iso}, \boldsymbol{\lambda}^{\rm local}, \boldsymbol{\delta}) = \\ \chi^2_{\rm PAO} + \left(\frac{\delta_E^{\rm PAO}}{\sigma_{\rm E}^{\rm PAO}}\right)^2 + \\ + \left(\frac{\delta^{\rm PAO}_{\langle X_{\rm max}\rangle}}{100\%}\right)^2 + \left(\frac{\delta^{\rm PAO}_{\sigma(X_{\rm max})}}{100\%}\right)^2 + \\ \chi^2_{\rm TA} + \left(\frac{\delta_E^{\rm TA}}{\sigma_{\rm E}^{\rm TA}}\right)^2 + \\ + \left(\frac{\delta^{\rm TA}_{\langle X_{\rm max}\rangle}}{100\%}\right)^2 + \left(\frac{\delta^{\rm TA}_{\sigma(X_{\rm max})}}{100\%}\right)^2 .\end{aligned} \tag{5}$$

As we can see, this χ^2 value takes int both the energy spectrum and the composition observables with energy above $E_{\rm min} = 6\times10^9$ GeV from both experiments.

A simultaneous scan of all parameters $\boldsymbol{\lambda}^{\rm iso}$, $\boldsymbol{\lambda}^{\rm local}$ and $\boldsymbol{\delta}$ would be computationally expensive, so instead we divide it into two steps. First, we perform a scan of $\boldsymbol{\lambda}^{\rm iso}$,

[2] While ideally, we could draw additional information by making use of data subsets from the Northern Hemisphere, Southern Hemisphere, and the common declination band seen by both experiments, these data sets are currently not publicly available.

[3] Here we follow Huber et al. (2005, 2007), where similar methods have been successfully used to combine the data from multiple neutrino oscillation experiments.

assuming only an isotropic source population. We consider the spectral and composition data from PAO in our entire energy range, as well as TA data below 25 EeV. This allows us to constrain the isotropic source parameters $\boldsymbol{\lambda}^{\rm iso}$, as well as the systematic variables $\boldsymbol{\delta}$ of both PAO and TA. We scan a three-dimensional parameter grid in $\gamma^{\rm iso}\times R^{\rm iso}_{\rm max}\times m^{\rm iso}$ with $81\times61\times61$ elements. For each set of parameter values, we numerically simulate the propagation of the five different primary isotopes from the entire source population, as described previously. The result of the propagation for different values of the other parameters ($\mathcal{L}^{\rm iso}_{\rm CR}$ and the five $\boldsymbol{f}^{\rm iso}_A$ parameters) can be obtained by normalizing the spectra at Earth to PAO observations.

We then fit the TA data in the full energy range, assuming the experiment observes (1) the isotropic source distribution, with the parameter values $\boldsymbol{\lambda}^{\rm iso}$ previously obtained, and (2) a local source characterized by $\boldsymbol{\lambda}^{\rm local}$, which we now optimize. For that, we scan a fine grid in $\gamma^{\rm local}\times R^{\rm local}_{\rm max}\times D^{\rm local}$ with $40\times61\times80$ elements. For each set of parameter values we simulate the propagation of an UHECR spectrum composed of a single isotope $A^{\rm local}$ from the local source to Earth. The fluxes arriving at Earth from the local source are added to those from the best-fit isotropic source population, before fitting the TA data.

This two-step approach does not affect the results because above 30 EeV, where the experiments differ, the overall fit is driven mainly by the PAO spectrum (due to its lower uncertainties), and therefore depends primarily on the isotropic source population. The local source parameters can then be searched separately in step two, in order to optimize the fit to high-energy TA data.

This method differs from that employed by Heinze et al. (2019) in three aspects: 1) that work considered only the PAO spectrum and composition data, while we include TA data in the same fit; 2) that work considered only an isotropic source distribution, while we consider also the presence of a local source observed by TA; and 3) that work took into account only uncertainties in the energy scale, while we include also the uncertainties on $\langle X_{\rm max}\rangle$ and $\sigma(X_{\rm max})$.

Furthermore, for completeness, we also performed a fit of the model of an isotropic source population to TA data only. The results of this fit are discussed in App. D and compared to the main results of this study as well as the previous work by Heinze et al. (2019). As we will show, when fitting only TA data an isotropic source population is less favored than when fitting only PAO data (best-fit χ^2/d.o.f.=1.6 vs. 1.3). The joint fit obtained in the main part of this paper leads to a higher value of χ^2/d.o.f.=1.7. As discussed in greater detail in Sec. 3, this is simply due to the inclusion of data from both experiments, which does not allow for a lower chi-squared value regardless of the model being fitted.

3. RESULTS AND DISCUSSION

In order to judge our hypothesis of a local UHECR source, we test two scenarios: 1) the null hypothesis that both TA and PAO observe the same isotropic source population, and 2) the hypothesis that TA additionally observes a local source in the Northern Hemisphere. Both scenarios are evaluated using the joint fit method described in Sec. 2, considering both TA and PAO data, and assuming constant systematic energy shifts, which are also optimized as part of the fit.

In Fig. 2 we show the best-fit results of both scenarios, obtained using Sibyll as the air shower model. On the left-hand side we show the case without a local source, and on the right-hand side the case where there is a local source in the Northern Hemisphere. In this case, the source emits silicon-28 and lies at a distance of 13.9 Mpc, which corresponds to the best fit found. The exact values and uncertainties of the best-fit parameters of the isotropic population, the local source, and the systematic energy shifts are provided in Tab. 1 for silicon-28. For other emitted isotopes there is a dedicated table in App. B.

The upper plots of Fig. 2 show the predicted cosmic-ray spectra. Focusing first on the data, we plot as black data points the energy-shifted PAO spectrum, and as brown points the TA spectrum. The best-fit energy shift values are provided in Tab. 1. As expected, the relative systematic shift between the energy scales, $\delta^{\rm PAO}_E - \delta^{\rm TA}_E$, is consistent with the previous analysis by Tsunesada et al. (2021). The absolute values of $\delta^{\rm PAO}_E$ and $\delta^{\rm TA}_E$ differ from that study because there they were chosen to be symmetric, while here they were obtained through the joint fit to our model. Like in Fig. 1, this shift leads to an agreement between the spectra from the two experiments up to about 30 EeV, while above that energy the TA fluxes are generally higher. For reference, we show as a dashed line the threshold energy of 25 EeV above which the new excess was found in the TA data (Abbasi et al. 2021a).

The dashed black curves represent the contribution of the isotropic source population, which is observed by both experiments. The contributions from the different mass groups are shown in different colors. In the top right plot, we show in addition as a solid black curve the total contribution from the local source that emits silicon-28. This contribution is almost entirely within the silicon mass group also at Earth, as indicated by the solid yellow curve that can be seen behind the black

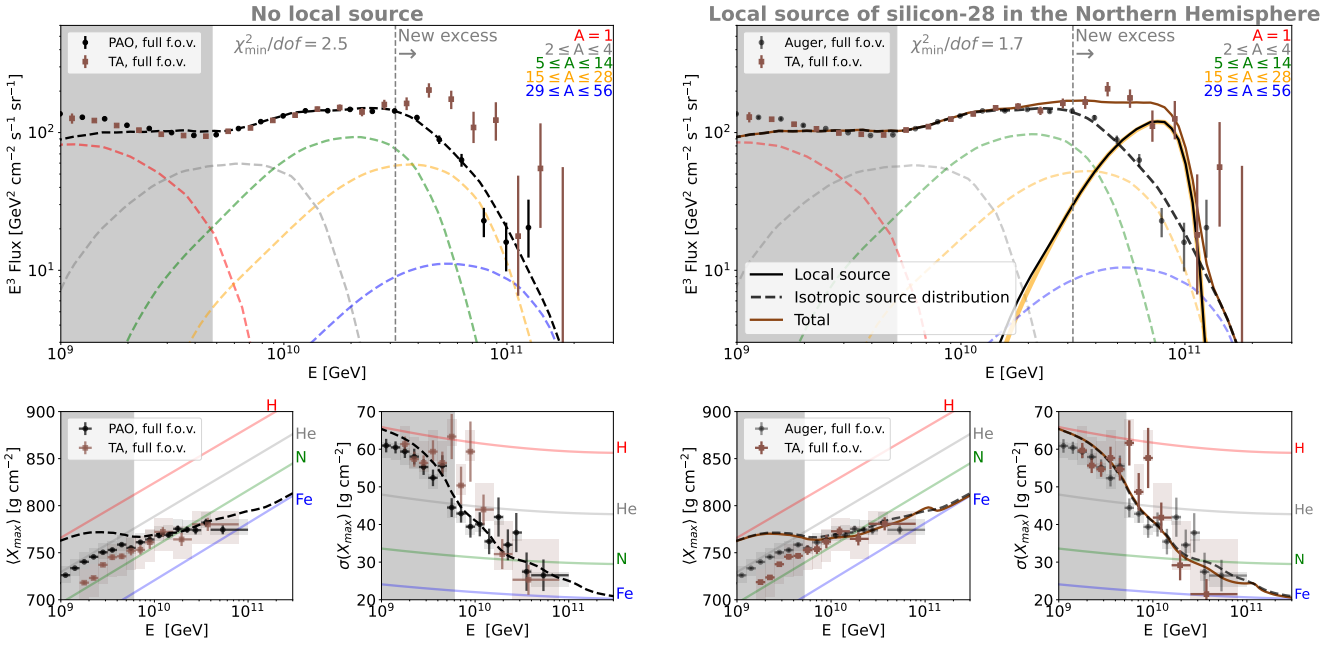

Figure 2. Spectra (upper panels) and composition observables (lower panels) resulting from a joint fit to TA and PAO data, using Sibyll 2.3c as the air shower model. In the left plots, we show the best fit considering only an isotropic source population, and in the right considering additionally the presence of a local source of silicon-28 in the Northern Hemisphere. We assume an energy-independent shift in the energy scales of the experiments, whose values are given in Tab. 1 together with the other best-fit parameters. The gray shaded energy ranges are not included in the fit.

curve. Finally, the brown curve represents the sum of the isotropic population and the local source, which is the total flux observed by TA.

The first thing to note is that the best-fit spectrum from the isotropic source population is similar in both cases, although in the left-hand plot that isotropic component is fitted to data from both experiments and in the right-hand plot only to PAO. This is because at higher energies, where the PAO and TA spectra are discrepant, the TA data have considerably larger uncertainties, and therefore the fit of the isotropic component is driven by the PAO data in either scenario. This can also be seen by comparing the left- and right-hand columns of Tab. 1, where the parameters of the source population are in fact similar in both scenarios.

Comparing the best-fit results with data, we can see that in the left panel the isotropic source population alone fails to explain TA data above 30 EeV, and the overall joint fit has a high value of 109.1/44 = 2.5 per degree of freedom (d.o.f.), which includes also the composition data in the bottom plots.

In contrast, the model on the right-hand side has a lower value of χ^2/d.o.f.=1.7, because the tension with TA data is explained by the additional flux from the local source. While in the scenario without a local source the large value of χ^2/d.o.f. was mainly due to the tension with the TA spectrum data at high energies, in this case, the fit cannot be further improved due to the low uncertainties of the PAO and TA spectra at energies below $\sim$ 20 EeV. Even by optimizing the energy shift, the data from both experiments cannot be brought to a more precise agreement at these low energies, which necessarily limits the quality of any joint fit. This is in contrast with the PAO-only fit by Heinze et al. (2019), who obtained a lower χ^2/d.o.f.=1.3.

The composition observables are shown in the bottom plots of Fig. 2. Regarding the isotropic source distribution, as reported in Tab. 1, the best-fit composition is dominated by helium at the 80-90% level, followed by nitrogen. This is consistent with previous fits to PAO data only by Heinze et al. (2019) and Aab et al. (2017). That means that the addition of the TA data does not considerably change predictions on the composition emitted by the sources. On the other hand, the content of protons emitted directly by the sources cannot be constrained because their maximum energy lies below the minimum energy threshold of our fit. This is due to the assumption of a rigidity-dependent maximum energy for the emitted cosmic rays, as described in Sec. 2.

Regarding the local source, we can see that its contribution does not change considerably the expected values of $\langle X_{\rm max}\rangle$ and $\sigma(X_{\rm max})$ above our fitting threshold (compare dashed black curves and solid brown curves in the bottom-right panels of Fig. 2). Out of the five

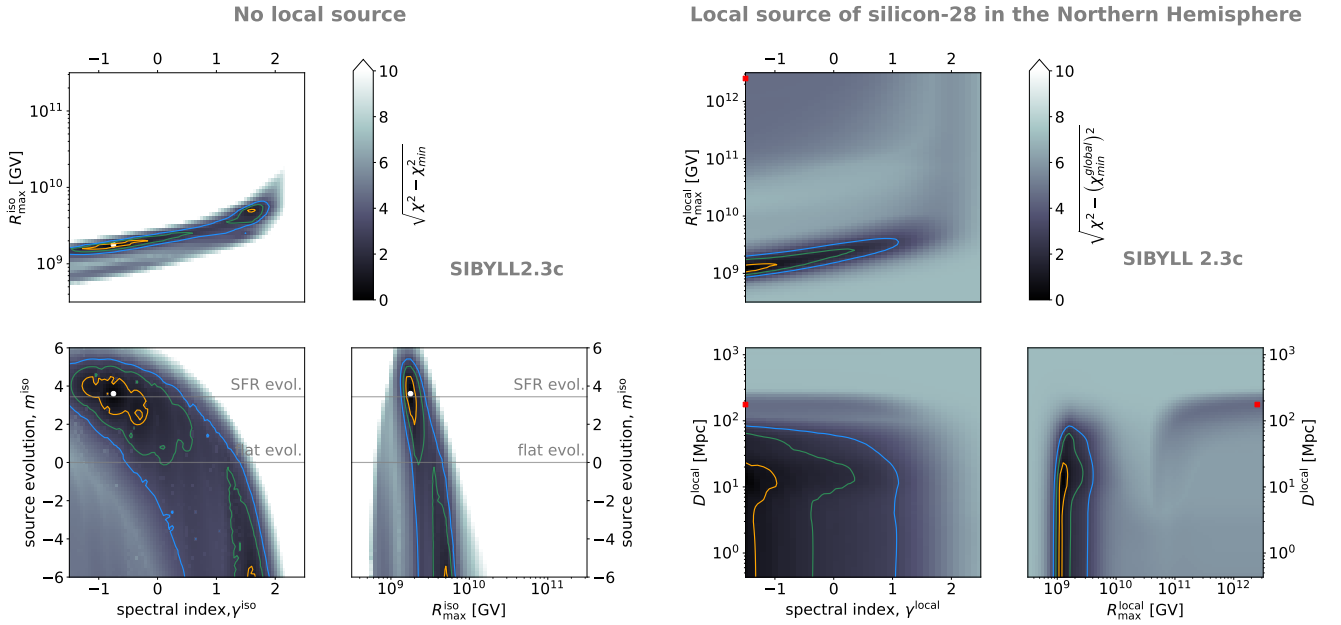

Figure 3. *Left:* A portion of the parameter space of an isotropic source population, based on a joint fit to TA and PAO data, assuming both experiments observe only this isotropic source population. *Right:* Assuming that additionally to an isotropic source population there exists also a local source of silicon-28 in the Northern Hemisphere (observed only by TA), we show here a portion of the parameter space of that local source, also based on a joint fit. The best-fit parameters of either scenario (also listed in Fig. 2) are marked here by white dots, while another minimum, representing an extreme accelerator, is marked by red squares. The colored shading corresponds to the χ^2 value compared to the best fit, while the yellow, green and blue contours indicate the 1-, 2- and 3σ regions, respectively, calculated for two d.o.f. In each panel, the parameter that is not shown is treated as a nuisance parameter and minimized over. SIBYLL 2.3c was used as the air shower model.

isotopes we tested, silicon provides the best overall fit quality for SIBYLL and EPOS-LHC, and nitrogen for QGSJET. However, scenarios where the local source emits other isotopes are also viable. As discussed later in this section and in more detail in App. B, heavier isotopes, such as iron, lead to results that fit the data only marginally worse than silicon, and require that the source lie farther from Earth. On the other hand, as shown in App. B, considerably lighter isotopes, such as protons and helium, provide comparatively poor fits to data, because the predicted composition at Earth is too light compared to TA data.

Because the two scenarios of Fig. 2 are essentially nested models (i.e. they are equal with the exception of a local source that adds a set of independent parameters), we can compare them directly using Wilks' theorem (Wilks 1938). We then conclude that, under the assumption of a constant systematic energy shift in both TA and PAO, the existence of a local source in the Northern Hemisphere is favored at the 5.6σ level compared to the model where there is only an isotropic source population. The other air shower models also lead to a result with high significance, as detailed in the bottom row of Tab. 1.

In App. A we explore how our assumption on the experiment systematics may affect this result. Specifically, we test the more complex case where the energy shifts in both experiments are not energy-dependent, as proposed recently by the TA and PAO working group Tsunesada et al. (2021). We show that in that case, the presence of a local source is neither favored nor disfavored, because the discrepancies between the full f.o.v. spectra at high energies become smaller, and the fit is no longer sensitive to the effect of the local source. However, as shown in App. A, our baseline model with a local source and energy-independent experiment systematics can provide a better joint fit than a scenario involving energy-dependent systematics and is favored at level 4.4σ. This again supports the idea that the high-energy flux differences may originate at least partially from an astrophysical contribution, rather than purely from experiment systematics.

In Fig. 3 we show the values of $\Delta\chi = \sqrt{\chi^2 - \chi^2_{\rm min}}$ for a region of the parameter space, where $\chi^2_{\rm min}$ is the best-fit chi-squared value. On the left, we can see the parameter space of the isotropic source population for the scenario without a local source. The white dots represent the best-fit parameters, which correspond to the

result in the left panel of Fig. 2. The yellow, green, and blue contours represent the regions 1, 2, and 3σ away from the best fit. These source population parameters are compatible with the result by Heinze et al. (2019), although only PAO data were fitted in that work. As mentioned above, the reason for this is that at higher energies, where the experiments observe different fluxes, PAO data has significantly lower statistical uncertainties, and therefore drives the fit.

On the right panel of Fig. 3 we show the parameter space of the local source in the full model, assuming silicon-28 emission, with the white dots representing the best-fit result (as on the right-hand side of Fig. 2). As we can see, the strictest constraint obtained is on the maximum rigidity of the cosmic rays accelerated by the local source, $R_{\rm max}^{\rm local}$. As detailed further in App. B, the best-fit value of $E_{\rm max}^{\rm local} = Z_A\, R_{\rm max}$ does not depend on the isotope (or mix of isotopes) accelerated by the source. Another interesting feature of $R_{\rm max}^{\rm local}$ is that there are two ranges that can provide a good fit. The lower range, centered around 20 EeV, is the best-fit case shown in Fig. 2 (white dots); and for $E_{\rm max} > 2000$ EeV, the model becomes viable again at the 2σ level. The best fit in this energy range is shown as a red square. This second case represents a local source that is an extreme accelerator of cosmic rays up to the ZeV regime. In this scenario, the ZeV cosmic rays from the local source disintegrate efficiently into protons and simultaneously cool down to tens of EeV, leading to a pure-proton component at Earth that explains the TA excess. As we can see in the bottom-right plot, the local source must lie at a distance of at least 100 Mpc in order for this strong cooling to occur. Although for Sibyll this "exotic" is at best 2σ away from the best-fit case, when considering Epos-LHC there is in fact a viable solution within the 1σ region. These details are discussed further in App. C.

Regarding the spectral index of the cosmic rays emitted by the local source, we can see that our result can only provide an upper limit of $\gamma^{\rm local} < 0.5$. This is because softer spectra would lead to an additional flux at Earth below 20 EeV that would overshoot the observed TA flux. On the other hand, a lower limit of $\gamma^{\rm local}$ cannot be obtained because for hard spectra the flux becomes dominated by cosmic rays with energy close to $E_{\rm max}$, and therefore the precise shape of the distribution cannot be constrained.

Finally, we can see that the distance to the local source is also constrained. To better illustrate this, we show in the left panel of Fig. 4 the 1σ and 3σ uncertainty regions on the distance traveled by the cosmic rays from the local source to Earth, for five different emitted isotopes. All other parameters are kept at their best-fit values. Silicon-28 was the case discussed so far, which provides the best fit out of the five mass groups. Assuming Sibyll as the air shower model (blue, cf. also Tab. 1), the source should lie at any distance below 23.1 Mpc for a result within the 1σ region, with the best fit obtained for 13.9 Mpc. This constraint on the distance arises from the optimal efficiency of photodisintegration undergone by silicon nuclei at the highest energies that is necessary to explain the data.

In the right plot of Fig. 4 we show the energy loss length for silicon (yellow curve) and, as a reference, the energy range relevant for our fit (orange band): from 6 EeV, the minimum energy of the joint fit, up to 224 EeV, the highest energy for which TA provides a flux measurement. As we can see, the energy loss length of a silicon nucleus with an energy of $\sim$200 EeV is roughly 10 Mpc, which is the same order of magnitude as our optimal local source distance of 14 Mpc. If the local source were to lie much closer to Earth, the emitted silicon nuclei would undergo less photodisintegration, leading to an observed TA flux with a harder spectrum and heavier composition. However, as we can see in the left-hand plot, in that case, we are still able to explain observations within the 1σ region of the best fit. On the other hand, if the source were to lie at a distance much larger compared to the energy loss length, efficient photodisintegration at these energies would be too thorough, producing large amounts of secondary nuclei. These lighter isotopes should then be observed by TA at lower energies (due to their lower mass number), leading to an additional flux that is not supported by the data. For that reason, distances much larger than $\sim$ 10 Mpc are excluded for the case of silicon.

By the same token, for a lighter element like nitrogen, the maximum distance to the source becomes limited to about 1 Mpc, as we can see on the left-hand-side plot, while for heavier isotopes like iron it is much larger, of order 100 Mpc. All these cases can be understood by noting the different curves of the right-hand plot, as the optimal distance to the source corresponds roughly to the energy loss length of the respective isotope at the highest energy.

As shown in Fig. 4, Andromeda (M31) lies at a distance of 752 kpc. Our neighboring galaxy is therefore in principle viable as a local UHECR source in the case of intermediate-mass isotopes like nitrogen and silicon. On the other hand, a source such as the Perseus-Pisces supercluster (PPS, also known as A 426), at 70 Mpc, would satisfy the distance criterion for isotopes in the iron group. Both these objects are also supported as possible local source candidates by current data from TA, since their position is compatible with the direction

of the high-energy excess recently detected (Kim et al. 2021). Additionally, other candidate sources may also of course exist. Possible candidates may even lie outside the region of the new excess, due to cosmic-ray deflections by the Galactic magnetic fields (GMFs); see also discussion below.

In terms of energetics, as detailed in Tab. 1 and Tab. 3 in App. B, the necessary cosmic-ray luminosity of a source that emits nitrogen is 10^{39} erg/s. For an iron source, we need a luminosity of 5.5×10^{43} erg/s, which is higher due to the larger distance required. Both Andromeda and the PPS have higher total photon luminosities (10^{44} erg/s and 8×10^{44} erg/s (Boehringer et al. 2021), respectively), which means that they may be feasible candidates within this model from the energetics point of view. In the case of Andromeda, a very low cosmic-ray loading of 10^{-5} would be sufficient to explain observations. On the other hand, being a spiral galaxy, the question would still remain of what are the acceleration sites of such energetic cosmic rays, which is however outside the scope of this work.

In general, large-scale structured GMFs will cause a shift in the position in the sky of the UHECR source. On the other hand, the presence of small-scale turbulent GMFs leads to a spreading effect around the source position (see e.g. Shaw et al. (2022)). This spreading effect needs to be small enough for the local UHECR source in the Northern Hemisphere in order not to affect our declination-dependent interpretation of the spectrum. The amount of spread around the (potentially shifted) source position can be estimated as (see e.g. Lee et al. (1995)):

$$\begin{aligned}\theta_{\mathbf{rms}} \approx & \frac{2}{\pi}\sqrt{D\lambda_B}\frac{ZeB}{E} \\ \approx & 0.35^\circ Z \left(\frac{D}{10\ \mathbf{kpc}}\right)^{1/2} \left(\frac{\lambda_B}{100\ \mathbf{pc}}\right)^{1/2} \\ & \times \left(\frac{B}{1\ \mu\mathbf{G}}\right)\left(\frac{E}{100\ \mathbf{EeV}}\right)^{-1}, \end{aligned} \tag{6}$$

with D the distance through the Galaxy where these turbulent magnetic fields are present, λ_B the correlation length of the turbulent magnetic fields and B the magnetic-field strength. For silicon-28 with an energy of 30 EeV, and typical order-of-magnitude magnetic-field parameters of $D = 10$ kpc, $\lambda_B = 100$ pc and $B = 1$ μG, this gives $\theta_{\mathbf{rms}} \approx 16^\circ$, which is roughly consistent with the extent of the new excess found by TA. However, note that the extent of the turbulent magnetic fields in our Galaxy, their correlation length and their strength are not well known. If they happen to be significantly stronger or wider spread than the order-of-magnitude estimates given here, the expected UHECR spreading increases significantly. In such a scenario, a lighter composition than silicon might be favorable.

4. SUMMARY AND CONCLUSIONS

We have performed a joint fit to current PAO and TA data accounting for both spectra and composition observables; we have been using the standard rigidity-dependent maximal energy model considering all relevant parameters including their multi-parameter correlations. We have tested the hypothesis that both experiments observe an isotropic distribution of equal UHECR sources, while TA observes an additional local UHECR source located in the Northern Hemisphere. We have demonstrated that the presence of the local source is favored at the 5.6σ level compared to the null hypothesis of an isotropic sky.

Our best joint fit reveals a local source that emits cosmic rays dominated by the silicon-28 mass group, with a hard spectrum ($\gamma^{\rm local} < -1.0$) and a maximum energy of $E^{\rm local}_{\rm max} = 20$ EeV. Although the best fit is obtained considering Sibyll 2.3c as the air shower model, good fits can also be obtained when considering QGSJET-II-04 and Epos-LHC – which we have also tested. Besides silicon, other isotopes with masses between nitrogen and iron are also viable within the 3σ region relative to the best fit (cf. App. B). In the silicon scenario, the source must lie within a distance of 14 Mpc, making Andromeda a viable candidate. For heavier elements such as iron, the local source should lie at a distance of the order of 100 Mpc, compatible with an object such as the Perseus-Pisces supercluster. Both source candidates have a photon luminosity higher than the cosmic-ray luminosity required by the model, making them energetically viable. Furthermore, both lie within the angular uncertainty region of the flux excess recently reported by TA (Kim et al. 2021); our model predicts that their contribution should be dominant above 30 EeV, which is approximately the energy range of the TA excess.

While we have derived our main result using standard systematic shifts of the energy grids of the PAO and TA experiments (independent of energy), we have compared to a scenario where the differences in the measurements may originate from systematic energy-dependent shifts in the energy grids of the two experiments; see App. A for details. We have demonstrated that the astrophysical explanation (the local UHECR source) leads to a significantly better goodness of fit versus the tested systematics explanation (χ^2/d.o.f. = 1.7 versus 2.5 com-

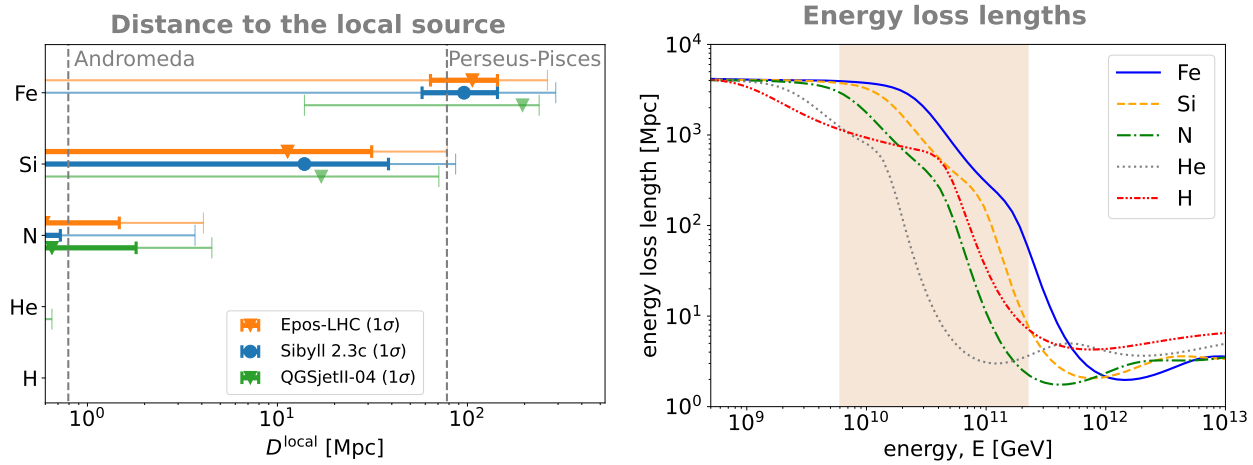

Figure 4. *Left:* Best-fit results on the travel distance of the cosmic rays emitted by the local source, depending on the emitted isotope, in the 1σ region (bold error bars) and 3σ (thin error bars), for one degree of freedom. The colors refer to the three different air shower models. *Right:* Energy loss lengths (for redshift $z = 0$) of the four tested isotopes as a function of the nucleus energy. This includes adiabatic cooling, photopair production, photopion production and photodisintegration off the CMB and EBL (Heinze 2020). The orange band shows the energy range relevant for the joint fit.

pared to the null hypothesis of standard systematics and isotropic sky). Note, however, that the local UHECR source cannot be significantly established on top, if the energy-dependent shifts are present. One may speculate that for slightly adjusted systematics both hypotheses may work equally work; such a systematics however requires a clear physical motivation.

We conclude that a local UHECR source provides a good description for the long-standing discrepancy of the spectrum and composition data between PAO and TA. While our 5.6σ significance with respect to the null hypothesis (isotropic sky, standard systematics) is high and this astrophysical explanation is clearly more attractive than a systematical one, the claim for a groundbreaking discovery probably requires a) a better understanding of possible energy-dependent systematics, b) a scrutinizing analysis performed by the experimental collaborations using updated data, and c) an unambiguous association with (possibly observed) anisotropies. On the modeling side, have we restricted ourselves to a single mass group from the local source due to the computational effort, while a more complex model involving a mix of isotopes may eventually provide a better joint fit, and constrain the properties of the local source further. However, the higher number of parameters of such a model will require higher statistics from the Northern Hemisphere, which can only be made possible by future experiments such as the planned TAx4 experiment (Abbasi et al. 2021b).

ACKNOWLEDGMENTS

The authors would like to thank Simone Garrappa and Domenik Ehlert for helpful discussions. This work was supported by the International Helmholtz-Weizmann Research School for Multimessenger Astronomy, largely funded through the Initiative and Networking Fund of the Helmholtz Association.

REFERENCES

Aab, A., et al. 2015, Nucl. Instrum. Meth. A, 798, 172, doi: 10.1016/j.nima.2015.06.058

Aab, A., Abreu, P., Aglietta, M., et al. 2017, Journal of Cosmology and Astroparticle Physics, 2017, 038, doi: 10.1088/1475-7516/2017/04/038

—. 2020, Phys. Rev. D, 102, 062005, doi: 10.1103/PhysRevD.102.062005

Abbasi, R. U., Abe, M., Abu-Zayyad, T., et al. 2014, The Astrophysical Journal, 790, L21, doi: 10.1088/2041-8205/790/2/l21

Abbasi, R. U., et al. 2018a. https://arxiv.org/abs/1801.07820

Abbasi, R. U., Abe, M., Abu-Zayyad, T., et al. 2018b, The Astrophysical Journal, 858, 76, doi: 10.3847/1538-4357/aabad7

Abbasi, R. U., et al. 2021a. https://arxiv.org/abs/2110.14827

—. 2021b, PoS, ICRC2021, 355, doi: 10.22323/1.395.0355

Abu-Zayyad, T., et al. 2013, Nucl. Instrum. Meth. A, 689, 87, doi: 10.1016/j.nima.2012.05.079

Table 1. Best-fit parameters corresponding to the results of the joint fit to PAO and TA. The 1σ uncertainty region is given for 1 d.o.f.

		Isotropic source distribution only			Isotropic source distribution + local source		
		Sibyll 2.3c	Epos-LHC	QGSJET-II-04	Sibyll 2.3c	Epos-LHC	QGSJET-II-04
Isotropic source distrib.	$\gamma^{\rm iso}$	$-0.75^{+0.15}_{-0.15}$	$0.10^{+0.05}_{-0.1}$	$-0.60^{+0.03}_{-0.05}$	$-0.75^{+0.15}_{-0.45}$	$-0.85^{+0.05}_{-0.05}$	$-0.65^{+0.05}_{-0.03}$
	$R^{\rm iso}_{\rm max}$ (GV)	$1.8^{+0.2}_{-0.2}\times10^9$	$2.5^{+0.2}_{-0.2}\times10^9$	$2.5^{+0.2}_{-0.2}\times10^9$.	$1.8^{+0.2}_{-0.2}\times10^9$	$2.0^{+0.2}_{-0.2}\times10^9$	$2.5^{+0.2}_{-0.2}\times10^9$
	$m^{\rm iso}$	$3.6^{+0.6}_{-0.6}$	< -4.8	< -5.8	$3.8^{+0.6}_{-0.6}$	$0.6^{+0.6}_{-0.6}$?	< -5.8
	$f_A(\%)$						
	H	$0.004^{+99.996}_{-0.004}$	$0.000^{+86.756}_{-0.000}$	$0.002^{+99.881}_{-0.002}$	$0.004^{+99.928}_{-0.004}$	$0.001^{+99.879}_{-0.001}$	$0.000^{+84.659}_{-0.000}$
	He	$86.096^{+1.986}_{-2.256}$	$88.799^{+0.329}_{-0.338}$	$92.588^{+0.258}_{-0.266}$	$80.504^{+4.150}_{-4.948}$	$92.125^{+0.485}_{-0.514}$	$92.471^{+0.261}_{-0.270}$
	N	$13.324^{+0.728}_{-0.696}$	$10.578^{+0.414}_{-0.400}$	$7.222^{+0.291}_{-0.281}$	$18.803^{+0.936}_{-0.901}$	$7.738^{+0.308}_{-0.298}$	$7.375^{+0.207}_{-0.202}$
	Si	$0.567^{+0.113}_{-0.094}$	$0.609^{+0.110}_{-0.093}$	$0.181^{+0.034}_{-0.028}$	$0.676^{+0.266}_{-0.192}$	$0.133^{+0.045}_{-0.034}$	$0.147^{+0.033}_{-0.027}$
	Fe	$0.010^{+0.008}_{-0.004}$	$0.015^{+0.017}_{-0.008}$	$0.007^{+0.003}_{-0.002}$	$0.012^{+0.012}_{-0.006}$	$0.003^{+0.003}_{-0.002}$	$0.005^{+0.002}_{-0.002}$
Loc. source	isotope				silicon-28	silicon-28	nitrogen-14
	$\gamma^{\rm local}$				< -1.0	< -1.1	< -1.1
	$R^{\rm local}_{\rm max}$ (GV)				$1.3^{+0.2}_{-0.1}\times10^9$	$2.3^{+0.3}_{-0.1}\times10^9$	$2.5^{+0.3}_{-0.3}\times10^9$
	$L^{\rm local}_{\rm CR}$ (erg s^{-1})				$1.1^{+2.0}_{-1.1}\times10^{42}$	$7.3^{+18.0}_{-7.3}\times10^{41}$	$< 1.0\times10^{40}$
	$D^{\rm local}$ (Mpc)				$13.9^{+9.2}_{-13.9}$	$11.3^{+9.5}_{-11.3}$	$< +1.4$
Systematics	$\delta^{\rm PAO}_E(\%)$	$-11.6^{+2.1}_{-0.5}$	$-8.97^{+1.1}_{-0.5}$	$10.8^{+0.0}_{-0.3}$	$-11.7^{+0.8}_{-1.5}$	$-9.5^{+0.5}_{-0.6}$	$10.9^{+0.9}_{-0.0}$
	$\delta^{\rm TA}_E(\%)$	$-20.5^{+1.9}_{-0.5}$	$-18.3^{+1.0}_{-0.4}$	$10.8^{+0.0}_{-0.3}$	$-19.7^{+0.7}_{-1.3}$	$-17.6^{+0.5}_{-0.6}$	$1.1^{+0.8}_{-0.00}$
	$\delta^{\rm PAO}_{\langle X_{\rm max}\rangle}(\%)$	-25^{+25}_{-27}	-100^{+0}_{-0}	-100^{+0}_{-0}	-26^{+26}_{-23}	-100^{+0}_{-0}	-100^{+0}_{-0}
	$\delta^{\rm TA}_{\langle X_{\rm max}\rangle}(\%)$	18^{+12}_{-12}	-18^{+5}_{-3}	-47^{+2}_{-0}	22^{+13}_{-11}	-12^{+4}_{-5}	-31^{+0}_{-2}
	$\delta^{\rm PAO}_{\sigma(X_{\rm max})}(\%)$	50^{+26}_{-30}	-59^{+15}_{-9}	100^{+0}_{-0}	56^{+27}_{-24}	-73^{+11}_{-11}	100^{+0}_{-0}
	$\delta^{\rm TA}_{\sigma(X_{\rm max})}(\%)$	-41^{+7}_{-9}	-90^{+4}_{-2}	3^{+3}_{-0}	-83^{+10}_{-9}	-100^{+0}_{-0}	-9^{+0}_{-3}
	χ^2/d.o.f.	109.1/44	130.4/44	269.6/44	67.6/40	87.8/40	239.6/40
	Favored vis-a-vis isotropic-only				5.6σ	5.7σ	4.6σ

Batista, R. A., de Almeida, R. M., Lago, B., & Kotera, K. 2019, Journal of Cosmology and Astroparticle Physics, 2019, 002, doi: 10.1088/1475-7516/2019/01/002

Bergman, D. 2019, PoS, ICRC2019, 190, doi: 10.22323/1.358.0190

Biehl, D., Boncioli, D., Fedynitch, A., & Winter, W. 2018, Astron. Astrophys., 611, A101, doi: 10.1051/0004-6361/201731337

Boehringer, H., Chon, G., & Truemper, J. 2021, Astron. Astrophys., 651, A16, doi: 10.1051/0004-6361/202140864

de Souza, V. 2017, PoS, ICRC2017, 522, doi: 10.22323/1.301.0522

Deligny, O. 2019, PoS, ICRC2019, 234, doi: 10.22323/1.358.0234

Gilmore, R. C., Somerville, R. S., Primack, J. R., & Domínguez, A. 2012, Monthly Notices of the Royal Astronomical Society, 422, 3189, doi: 10.1111/j.1365-2966.2012.20841.x

Heinze, J. 2020, PhD thesis, Humboldt-Universität zu Berlin, Mathematisch-Naturwissenschaftliche Fakultät, doi: http://dx.doi.org/10.18452/21386

Heinze, J., Fedynitch, A., Boncioli, D., & Winter, W. 2019, The Astrophysical Journal, 873, 88, doi: 10.3847/1538-4357/ab05ce

Huber, P., Kopp, J., Lindner, M., Rolinec, M., & Winter, W. 2007, Comput. Phys. Commun., 177, 432, doi: 10.1016/j.cpc.2007.05.004

Huber, P., Lindner, M., & Winter, W. 2005, Comput. Phys. Commun., 167, 195, doi: 10.1016/j.cpc.2005.01.003

Ivanov, D. 2017, PoS, ICRC2017, 498, doi: 10.22323/1.301.0498

—. 2019, PoS, ICRC2019, 298, doi: 10.22323/1.358.0298

Kim, J., Ivanov, D., Kawata, K., Sagawa, H., & Thomson, G. 2021, PoS, ICRC2021, 328, doi: 10.22323/1.395.0328

Koning, A. J., Hilaire, S., & Duijvestijn, M. C. 2007, in Proceedings, International Conference on Nuclear Data for Science and Tecnology, 211–214

Kotera, K., Amato, E., & Blasi, P. 2015, Journal of Cosmology and Astroparticle Physics, 2015, 026, doi: 10.1088/1475-7516/2015/08/026

Lee, S.-j., Olinto, A., & Sigl, G. 1995, Astrophys. J. Lett., 455, L21, doi: 10.1086/309812

Ostapchenko, S. 2011, Phys. Rev. D, 83, 014018, doi: 10.1103/PhysRevD.83.014018

Pierog, T., Karpenko, I., Katzy, J. M., Yatsenko, E., & Werner, K. 2015, Phys. Rev. C, 92, 034906, doi: 10.1103/PhysRevC.92.034906

Riehn, F., Engel, R., Fedynitch, A., Gaisser, T., & Stanev, T. 2016, PoS, ICRC2015, 558, doi: 10.22323/1.236.0558

Rodrigues, X., Fedynitch, A., Gao, S., Boncioli, D., & Winter, W. 2018, Astrophys. J., 854, 54, doi: 10.3847/1538-4357/aaa7ee

Shaw, V., van Vliet, A., & Taylor, A. M. 2022. https://arxiv.org/abs/2202.06780

Tokuno, H., et al. 2012, Nucl. Instrum. Meth. A, 676, 54, doi: 10.1016/j.nima.2012.02.044

Tsunesada, Y., Abbasi, R., Abu-Zayyad, T., et al. 2021, PoS, ICRC2021, 337, doi: 10.22323/1.395.0337

Verzi, V. 2019, PoS, ICRC2019, 450, doi: 10.22323/1.358.0450

Wilks, S. S. 1938, Annals Math. Statist., 9, 60, doi: 10.1214/aoms/1177732360

Yushkov, A. 2019, PoS, ICRC2019, 482, doi: 10.22323/1.358.0482

APPENDIX

A. COMPARISON WITH THE HYPOTHESIS OF AN ENERGY-DEPENDENT SHIFT

In the main text, we have accounted for systematic effects between the data from both experiments by introducing constant energy shifts to the spectrum and to the composition-related observables. We showed that the hypothesis that TA observes a local source in the Northern Hemisphere is significantly favored compared to the scenario where both experiments observe the same isotropic source population. We now address the hypothesis that there are systematic energy shifts in the two experiments that are themselves energy-dependent, $\delta_E^{\rm PAO}(E)$ and $\delta_E^{\rm TA}(E)$, and discuss the possible role of a local source in that scenario. As shown recently by Tsunesada et al. (2021), the discrepancy in the spectrum observed by the two experiments, considering only data from their common declination band, can be eased if the PAO spectral data is shifted by +4.5% and an additional +10%/decade above 10^{19} eV, and TA data by −4.5% and an additional −10%/decade above 10^{19} eV. Interestingly, however, when the same energy-dependent shift is applied to the data from outside the common declination band of the two experiments, the spectra are still discrepant above 30 EeV. This is shown in Fig. 5, where we plot three data sets: PAO data from its full field of view (f.o.v., black), TA data from its full f.o.v. (brown), and TA data from the northernmost declination band (red). These data points already contain the above-mentioned energy-dependent shifts for their respective experiment. We can see that above some 40 EeV the TA fluxes (both from the full f.o.v. and from the northernmost sky) are higher than those from the PAO, indicating an excess just like with the simpler assumption of an energy-independent shift (Fig. 1). This suggests that either the experiment systematics are declination-dependent (which seems to be disfavored, Tsunesada et al. 2021), or this effect is in fact astrophysical, as we argue in this paper.

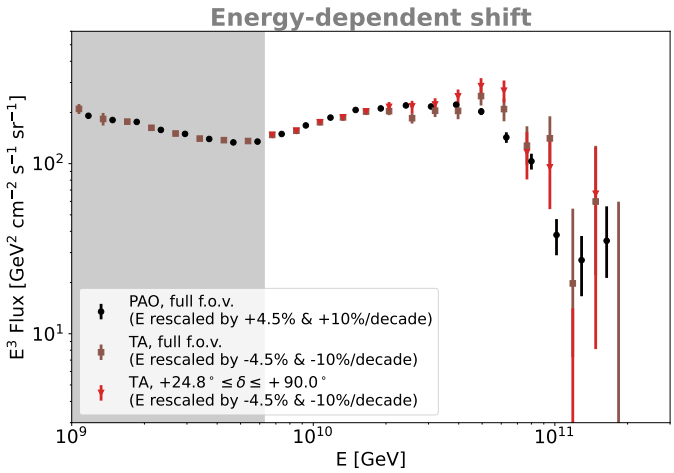

Figure 5. Energy spectrum of the UHECRs as measured by PAO full f.o.v (black circles), TA full f.o.v (brown squares), and TA Northernmost declination band (red triangles). Here, the energy scales of either experiment have been shifted by an energy-dependent amount, as described in the legend. With this energy-dependent shift, the spectra are compatible in the common declination band. However, as we can see, when considering other declination bands, there is an excess in the TA data compared to the PAO above ∼40 EeV, similarly to the case with an energy-independent shift discussed in the main text. Data from Tsunesada et al. (2021) and Deligny (2019).

Using the same method as in the main section of this work, we now test the scenario where the systematics in the energy grids of the two experiments are described by an energy-dependent shift (thus explaining the spectral difference in the common declination band), but a local source in the Northern Hemisphere also contributes to the flux observed by TA (explaining the differences that remain outside the common declination band). As in the main text, we start by testing the null hypothesis that there is no local source (i.e. a fully isotropic distribution), and perform a joint fit of the population parameters to the PAO and TA data, assuming the energy-dependent shift suggested by Tsunesada et al. (2021). Then, assuming the same energy-dependent shift, we test the hypothesis of a local source in the Northern

Hemisphere, and optimize the parameters of both the isotropic source distribution and the local source using the same search method as described in Sec. 2.3.

The best-fit results for these scenarios are shown in Fig. 6: on the left for the hypothesis of an isotropic source population, and on the right including a local source. In both cases, we consider Sybill as the air shower model, which, like in the main text, provides the best fit out of the three models tested. The best-fit parameter values are given in Tab. 2 for all three air-shower models. We also note a qualitative difference between this case and the main result of Fig. 2: here the best fit is obtained when the local source emits cosmic rays of the iron-56 mass group, rather than silicon-28 as in our main result.

Visually, the right-hand-side model seems to fit better the joint data at high energies; however, the two fits are actually characterized by the same value of χ^2/d.o.f.=2.2. This is because the fit is strongly driven by the low-energy spectral data, rather than the high energies where the local source contributes significantly. This is also the case of the joint fit performed in the main text, and is simply due to the lower uncertainties of the data at lower energies. In this case, however, an additional complication arises from the fact that the energy-dependent shift, which is optimized for the common declination band of both experiments, leads to discrepancies between the data from the full f.o.v., most noticeably between 20 and 30 EeV (compare black and brown data points in the upper panels of Fig. 6). As further discussed below, this discrepancy between the data sets is in fact one of the main factors behind the higher value of χ^2/d.o.f. obtained here compared to the scenario discussed the main text.

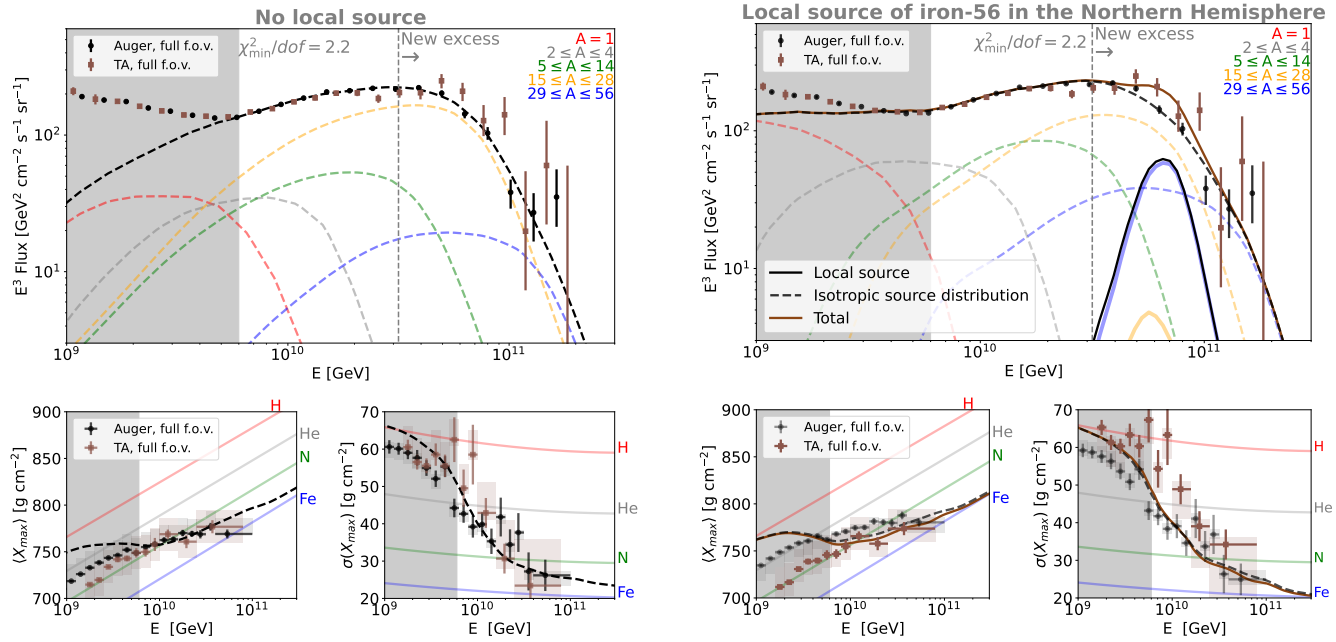

Figure 6. Spectra (upper panels) and composition observables (lower panels) resulting from a joint fit to TA and PAO data, using Sibyll 2.3c as the air shower model. Unlike the main result of Fig. 2, here we consider the systematics of the two experiments are given by the energy-dependent shift suggested by Tsunesada et al. (2021). On the left, we show the best fit considering only an isotropic source population, and on the right considering additionally the presence of a local source of iron-56 in the Northern Hemisphere. The corresponding parameters are provided in Tab. 2.

Let us now compare directly these results with the ones discussed in the main text. Turning our attention first to the left-hand panels of Fig. 2 and Fig. 6, we see that under the assumption of an isotropic source population, the existence of an energy-dependent shift is favored compared to an energy-independent shift (χ^2/d.o.f.=2.2 vs. 2.6). Even though the energy-dependent shift introduces two additional d.o.f. as well as discrepancies below 30 EeV in the full f.o.v. data, these factors are still out-weighed by the large excess in the TA flux that is observed assuming an energy-independent shift.

We can then compare the right-hand-side panels of Fig. 2 and Fig. 6, where a local source in the Northern Hemisphere is assumed. In this case, the energy-independent shift actually describes the full f.o.v. data better than an

energy-dependent shift (χ^2/d.o.f.=1.7 vs. 2.2), due to three factors: 1) an energy-independent shift requires two parameters less compared to the energy-dependent one, which increases the effective number of d.o.f. of the model; 2) the energy-independent shift also leads to a better agreement of the data below 30 EeV, where the spectral data has low uncertainties, allowing for the possibility of a better joint fit; and 3) with adequate parameters, the local source is capable of explaining the excess in the TA flux above 30 EeV equally well in either of the scenarios.

Overall, we can clearly say that among the four scenarios presented, the one with energy-independent systematics and a local source in the Northern Hemisphere provides the best joint fit to the full f.o.v. data from TA and PAO (χ^2/d.o.f.=1.7) and is favored at level 4.4σ compared to the case of the energy-dependent shift and assuming only an isotropic source population.

In Fig. 7 we show a region of the parameter space of the model assuming an energy-dependent shift for an isotropic source population only (left), and including the local source (right). As we can see on the left, the best-fit minimum (white dot) lies in a different region of parameter space compared to the energy-independent scenario tested in the main text (cf. left panel of Fig. 3). The best-fit parameters are listed in Tab. 2 for all three air-shower models considered. Compared to the main text case, this result requires a softer emission spectrum and a mildly negative source evolution ($m^{\rm iso} = -0.4$). As we can see by comparing the left-hand panels of Figs. 2 and 6, this negative source evolution means that photodisintegration is less effective, leading to a lower proton component; however, this fact does not affect the results since the proton component peaks below the energy threshold of this study.

Assuming Epos-LHC as the air-shower model we actually find three separate minima, and using QGSJET-II-04 only one minimum. Like in the case of Sibyll, for the sake of conciseness, we provide in Tab. 2 only the best-fit parameters, even in the cases where more than one minima are found.

Finally, as we can see by the white dots in the right panel of Fig. 7, and in Tab. 2, the local source has a similar value of the maximum rigidity $R^{\rm local}_{\rm max}$ for both the energy-independent and energy-dependent case, which underlines the fact that the TA excess is present at a similar energy. Other parameters are different: compared to the main text case we have iron instead of silicon, a much larger distance of ~ 200 Mpc (necessary for the more thorough disintegration of the iron nuclei, cf. App. B), and a higher luminosity of $\sim 10^{44}$ erg/s, which is simply due to the larger distance. As in Fig. 3, there is also a different local minimum corresponding to an extreme accelerator of ZeV cosmic rays (red squares), as discussed in more detail in App. C.

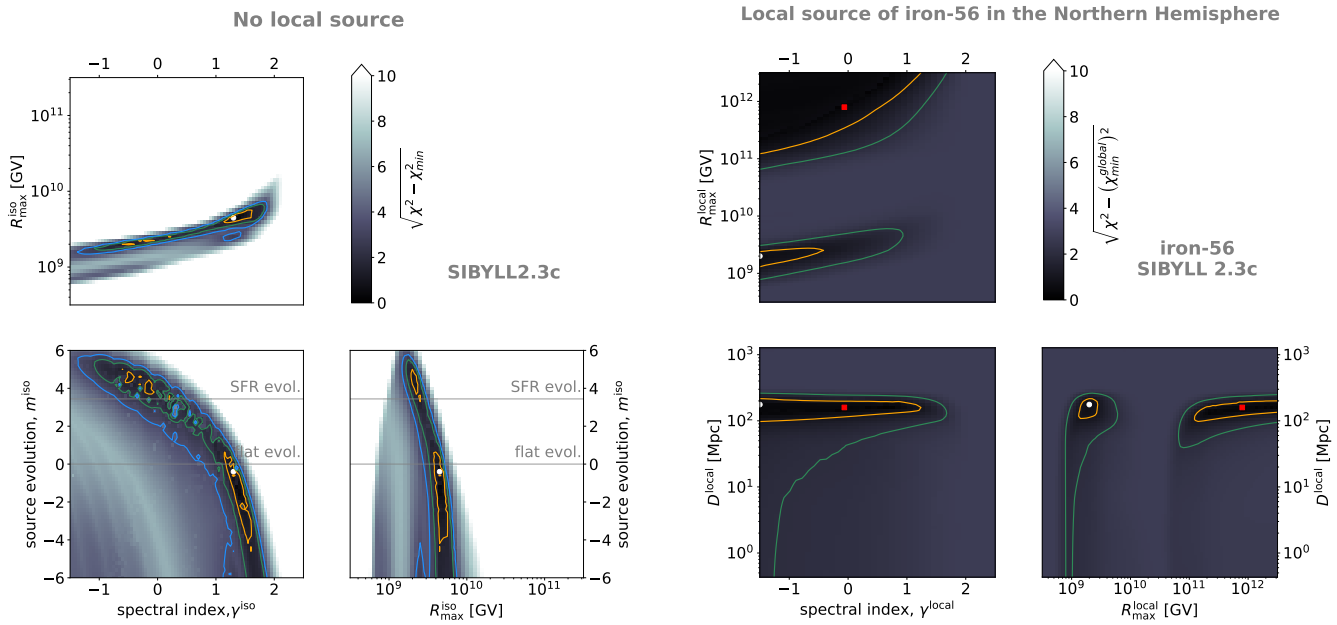

Figure 7. *Left:* Best-fit results for the joint fit to TA and PAO data, this time considering only an isotropic source population but allowing for energy-dependent energy shifts in the experiment energy scales. The best-fit point is marked by a white circle (case A); the second minimum is marked by a red square (case B). The best-fit parameters are provided in Tab. 2. *Right:* Parameter space for a local source for a joint fit to PAO and TA data when considering an isotropic source distribution, a local source in the Northern Hemisphere that emits cosmic rays of the iron-56 mass group, and additionally allowing energy-dependent shifts in the energy scales of the experiments. The best-fit parameters are shown as white dots; a second minimum, discussed in App. C, is marked with red squares. The meaning of the contour colors is as in Fig. 3.

Table 2. Best-fit parameters of the joint fit to PAO and TA, assuming energy-dependent systematic shifts in both experiments. The 1σ uncertainty ranges are given for 1 d.o.f.

		Isotropic source distribution only			Isotropic source distribution + local source		
		Sibyll 2.3c	Epos-LHC	QGSJET-II-04	Sibyll 2.3c	Epos-LHC	QGSJET-II-04
Isotropic source distrib.	$\gamma^{\rm iso}$	$1.30^{+0.15}_{-0.03}$	$-0.60^{+0.05}_{-0.05}$	$-0.65^{+-0.05}_{-0.05}$	$-0.55^{+0.45}_{-0.10}$	$-1.05^{+0.45}_{-0.05}$	$-0.70^{+0.03}_{-0.03}$
	$R^{\rm iso}_{\rm max}$ (GV)	$4.5^{+0.6}_{-0.3}\times10^9$	$2.2^{+0.3}_{-0.3}\times10^9$	$2.5^{+0.3}_{-0.3}\times10^9$	$2.0^{+0.2}_{-0.3}\times10^9$	$2.0^{+0.2}_{-0.2}\times10^9$	$2.5^{+0.2}_{-0.2}\times10^9$
	$m^{\rm iso}$	$-0.4^{+0.2}_{-1.6}$	$2.0^{+0.6}_{-0.8}$	< -6.0	$4.6^{+0.4}_{-0.8}$	$3.4^{+0.4}_{-1.8}$	< -6
	$f_A(\%)$						
	H	$0.003^{+99.996}_{-0.003}$	$0.002^{+98.898}_{-0.002}$	$0.002^{+99.646}_{-0.002}$	$0.016^{+99.981}_{-0.016}$	$0.000^{+97.389}_{-0.000}$	$0.001^{+99.997}_{-0.001}$
	He	$23.324^{+13.617}_{-9.683}$	$88.230^{+1.085}_{-1.180}$	$92.692^{+0.257}_{-0.265}$	$73.512^{+9.213}_{-11.849}$	$86.910^{+2.156}_{-2.506}$	$92.369^{+0.290}_{-0.300}$
	N	$36.272^{+6.781}_{-6.276}$	$11.055^{+0.600}_{-0.573}$	$7.102^{+0.220}_{-0.214}$	$23.306^{+2.116}_{-1.990}$	$12.557^{+0.633}_{-0.606}$	$7.450^{+0.228}_{-0.222}$
	Si	$38.957^{+2.691}_{-2.626}$	$0.693^{+0.099}_{-0.086}$	$0.198^{+0.035}_{-0.030}$	$3.072^{+0.414}_{-0.366}$	$0.524^{+0.079}_{-0.068}$	$0.174^{+0.036}_{-0.030}$
	Fe	$1.444^{+1.075}_{-0.620}$	$0.020^{+0.008}_{-0.006}$	$0.007^{+0.003}_{-0.002}$	$0.093^{+0.032}_{-0.024}$	$0.009^{+0.005}_{-0.003}$	$0.006^{+0.003}_{-0.002}$
Loc. source	isotope				iron-56	iron-56	iron-56
	$\gamma^{\rm local}$				< -0.3	< -0.2	< -0.5
	$R^{\rm local}_{\rm max}$ (GV)				$2.0^{+1.2}_{-0.2}\times10^9$	$1.8^{+0.7}_{-0.7}\times10^9$	$1.6^{+0.7}_{-0.3}\times10^9$
	$L^{\rm local}_{\rm CR}$ (erg s^{-1})				$1.3^{+1.1}_{-0.8}\times10^{44}$	$1.2^{+0.6}_{-1.0}\times10^{44}$	$5.4^{+7.7}_{-3.1}\times10^{43}$
	$D^{\rm local}$ (Mpc)				$176.2^{+39.4}_{-58.7}$	$176.2^{+18.7}_{-89.5}$	$130.1^{+46.1}_{-34.1}$
Systematics	$\delta^{\rm PAO}_{\langle X_{\rm max}\rangle}(\%)$	-100^{+0}_{-0}	-100^{+0}_{-0}	100^{+0}_{-0}	53^{+24}_{-18}	-100^{+0}_{-0}	-100^{+0}_{-0}
	$\delta^{\rm TA}_{\langle X_{\rm max}\rangle}(\%)$	-1^{+7}_{-4}	-7^{+4}_{-5}	46^{+3}_{-3}	-3^{+10}_{-8}	-7^{+5}_{-4}	-43^{+0}_{-0}
	$\delta^{\rm PAO}_{\sigma(X_{\rm max})}(\%)$	44^{+38}_{-9}	-79^{+11}_{-11}	-100^{+0}_{-0}	53^{+24}_{-18}	-91^{+18}_{-9}	100^{+0}_{-0}
	$\delta^{\rm TA}_{\sigma(X_{\rm max})}(\%)$	-62^{+10}_{-2}	-99^{+3}_{-1}	5^{+2}_{-2}	-3^{+10}_{-8}	-100^{+0}_{-0}	6^{+0}_{-0}
	χ^2 / d.o.f.	87.2 / 42	128.8 / 42	280.7 / 42	82.3 / 38	110.1 / 38	270.1 / 38

B. OTHER ISOTOPES

As discussed in Sec. 3, the isotope or mix of isotopes emitted by the local source cannot be directly constrained by our model, because this parameter is degenerate with the distance to the source. In the main result of Fig. 2 we limited the discussion to the case of silicon-28, which provides the best fit. However, other isotopes are also possible, as shown already in Fig. 4 and discussed in the text thereafter.

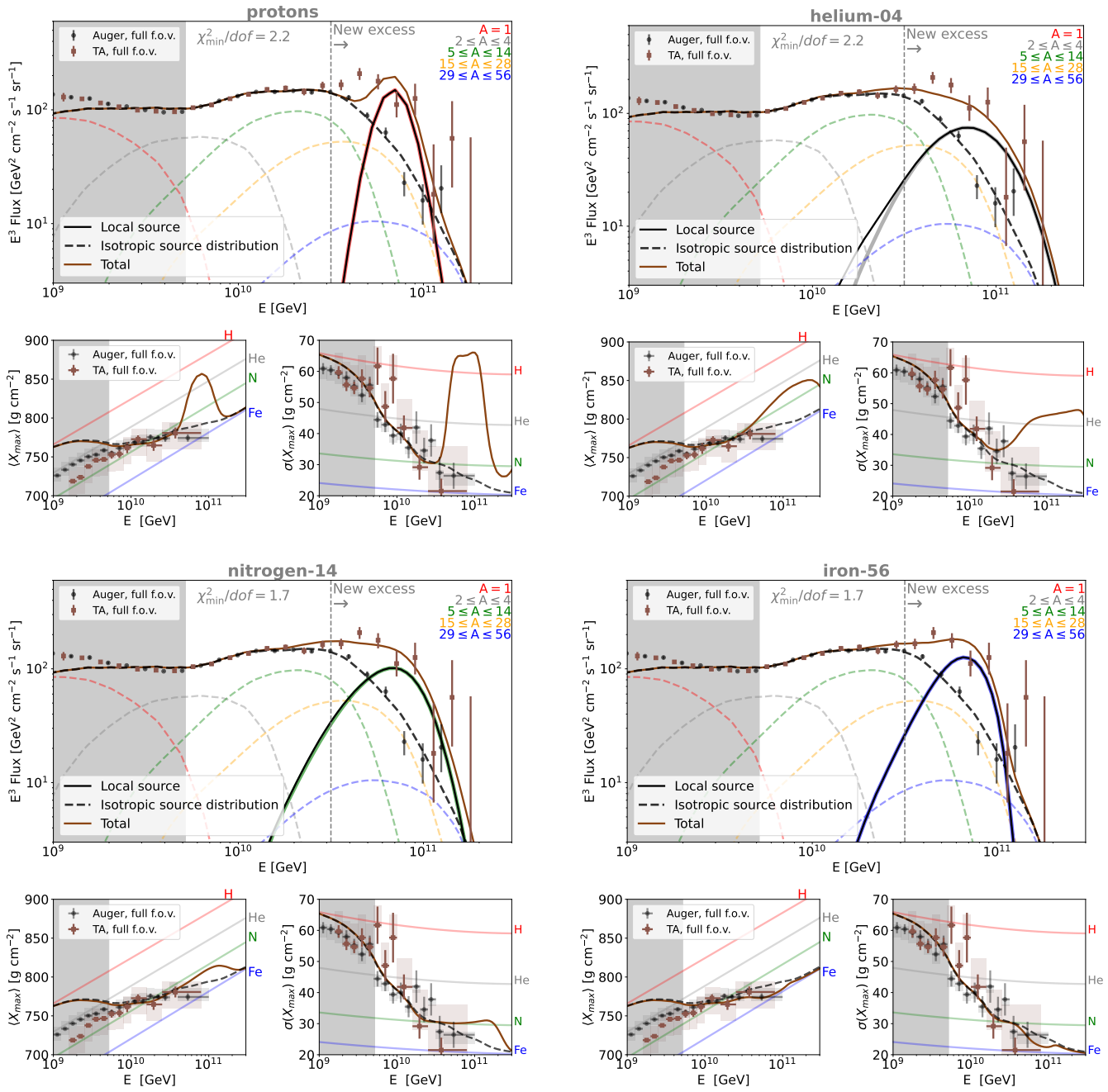

Figure 8. Spectra (upper panels) and composition observables (lower panels) predicted by the models, resulting from a joint fit to TA and PAO data when considering an isotropic source population and additionally a local source in the Northern Hemisphere, only observable by TA. The plots show the case where this local source emits protons (upper left), helium-04 (upper right), nitrogen-14 (lower left), and iron-56 (lower right). The gray shaded energy range was not included in the fit.

To further illustrate this, in Fig. 8 we show the best-fit results for the case where the local source emits protons (upper left), helium-4 (upper right), nitrogen-14 (lower left), and iron-56 (lower right). These results were obtained using Sibyll as the air shower model. Their respective best-fit distances were shown in the main part of this paper as blue points in the left panel of Fig. 4. We list the remaining best-fit parameters in Tab. 3, as well as for the other two air shower models tested.

As we can see, elements from any mass group up to iron-56 can provide results that are overall compatible with the joint data sets of PAO and TA, provided the emission characteristics and the source distance are adjusted according to Tab. 3. At the same time, some caveats should be noted for the different mass groups, as discussed below.

Emission of either protons or helium-4 leads to an observed composition that is light above 30 EeV, as we can see in the respective composition plots in Fig. 8. However, this does not affect the fit significantly because of the lack of composition data from either TA or PAO at these high energies. The case of a pure proton emission would lead to a result that is qualitatively similar to helium, with even larger values of $\langle X_{\rm max}\rangle$ and $\sigma(X_{\rm max})$ predicted for TA above 30 EeV.

For intermediate-mass isotopes like nitrogen-14, as well as heavier isotopes with mass up to iron-56, the composition observables exhibit the expected behavior with energy compared to our baseline scenario involving silicon, i.e. the observed composition becomes heavier with energy.

In all cases, we observe that the spectral data, rather than the composition observables, are the main factor driving the fit, due to their overall lower uncertainties. This means that with current statistics, we cannot point to any particular isotope (from the five mass groups up to iron-56) that leads to a significantly better joint fit.

Table 3. Best-fit parameters from the joint fit to PAO and TA data, assuming the emission of different isotopes from the local source. The best-fit values of the (energy-independent) systematic shifts are the same in all cases, and are given in Tab. 1.

	H	He	N	Si	Fe
Sibyll 2.3c					
$\gamma^{\rm local}$	< 0.3	< -1.2	< -1.2	< -1.0	< 0.3
$R^{\rm local}_{\rm max}$ (GV)	$> 9.0 \times 10^{10}$	$8.9^{+1.1}_{-0.3} \times 10^9$	$2.2^{+0.3}_{-0.3} \times 10^9$	$1.3^{+0.2}_{-0.2} \times 10^9$	$7.9^{+12.0}_{-0.1} \times 10^8$
$L^{\rm local}_{\rm CR}$ (erg s^{-1})	$7.6^{+14.7}_{-7.4} \times 10^{45}$	$< 1.0 \times 10^{39}$	$< 4.2 \times 10^{39}$	$1.1^{+2.0}_{-0.1} \times 10^{42}$	$5.5^{+22.0}_{-4.0} \times 10^{43}$
$D^{\rm local}$ (Mpc)	$176.2^{+18.7}_{-46.1}$	< 0.4	< 0.9	$13.9^{+9.2}_{-13.4}$	$95.9^{+99.0}_{-43.8}$
χ^2 / d.o.f.	88.3 / 40	87.4 / 40	69.3 / 40	67.6 / 40	69.1 / 40
Epos-LHC					
$\gamma^{\rm local}$	< 0.5	< -1.2	< -1.1	< -1.1	< 0.4
$R^{\rm local}_{\rm max}$ (GV)	$> 8.0 \times 10^{10}$	$8.9^{+1.1}_{-0.2} \times 10^9$	$2.5^{+0.3}_{-0.3} \times 10^9$	$1.3^{+0.3}_{-0.1} \times 10^9$	$8.9^{+11.0}_{-0.2} \times 10^8$
$L^{\rm local}_{\rm CR}$ (erg s^{-1})	$6.7^{+19.8}_{-6.4} \times 10^{45}$	$< 1.0 \times 10^{39}$	$< 1.9 \times 10^{39}$	$1.1^{+2.0}_{-0.1} \times 10^{42}$	$7.0^{+17.0}_{-5.0} \times 10^{43}$
$D^{\rm local}$ (Mpc)	$176.2^{+18.7}_{-32.3}$	< 0.4	< 1.2	$11.3^{+9.5}_{-10.9}$	$106.2^{+70.0}_{-48.5}$
χ^2 / d.o.f.	100.3 / 40	97.9 / 40	87.9 / 40	87.8 / 40	89.4 / 40
QGSJET-II-04					
$\gamma^{\rm local}$	< 0.6	< -1.2	$- < 1.1$	< -1.0	< -0.2
$R^{\rm local}_{\rm max}$ (GV)	$> 8.0 \times 10^{10}$	$8.9^{+1.1}_{-0.2} \times 10^9$	$2.5^{+0.3}_{-0.3} \times 10^9$	$1.4^{+0.4}_{-0.2} \times 10^9$	$1.6^{+0.7}_{-0.7} \times 10^9$
$L^{\rm local}_{\rm CR}$ (erg s^{-1})	$2.7^{+0.6}_{-2.1} \times 10^{46}$	$< 1.2 \times 10^{39}$	$2.4^{+7.7}_{-1.3} \times 10^{39}$	$1.6^{+2.3}_{-1.5} \times 10^{42}$	$3.2^{+1.5}_{-2.8} \times 10^{44}$
$D^{\rm local}$ (Mpc)	$194.9^{+10.2}_{-51.0}$	< 0.4	$0.7^{+0.7}_{-0.2}$	$17.0^{+8.6}_{-11.5}$	$194.9^{+20.7}_{-108.3}$
χ^2 / d.o.f.	252.8/ 40	247.7 / 40	239.6 / 40	242.3 / 40	246.1 / 40

C. AN "EXOTIC" SCENARIO: EXTREME LOCAL ACCELERATOR

As mentioned in the main text, additionally to our main result the parameter space of the local source contains another region that can provide a good joint fit to PAO and TA data. This is a scenario where the local source emits cosmic rays with extremely high maximum energies, above 10^{12} GeV.

An example of this kind of "exotic" solution was represented as red squares in the right-hand panel of Fig. 3, for the case where the local source emits cosmic rays of the silicon mass group, and considering Sibyll as the air shower model. However, as we demonstrate in this appendix, the extreme source can emit a composition dominated by any mass group. In the left panel of Fig. 9, we show as red squares the best-fit parameters of the extreme local source obtained for a pure proton composition and using Epos-LHC as the air shower model. In Tab. 4 we provide the complete list of the best-fit parameters of the extreme accelerator for different emitted mass groups and assuming different air shower models. As we can see, the best-fit parameters are close to those obtained in our baseline model (Fig. 3): a maximum energy of order ∼10 ZeV, a distance to the extreme local source of ∼100 Mpc, and a hard spectral index. The luminosity of the local source is similar regardless of the emitted isotope, as we can see in Tab. 4.

To understand these results we turn to the right-hand panel of Fig. 9, where we show the predictions for the spectrum and composition observables. These plots appear equal regardless of the emitted composition. As we can see, the ZeV cosmic rays emitted by the local source suffer strong photodisintegration due to the long distance traveled, to the point where the flux arriving at Earth is completely dominated by protons. These secondary protons carry approximately the same Lorentz factor as the primary nuclei emitted by the source, apart from energy loss processes like pair production and the adiabatic expansion of the Universe. Therefore, as long as the emitted cosmic rays peak at about 10 ZeV, the proton flux observed by TA will peak at a few tens of EeV, thus explaining the excess observed by TA like in the scenarios discussed previously.

Because in this scenario the local source contributes exclusively with protons to the TA spectrum, the result predicts a high value of $\langle X_{\rm max}\rangle$ and $\sigma(X_{\rm max})$ above a few tens of EeV in TA, as we can see in the bottom right-hand-side plots of Fig. 9. The only contribution of heavier cosmic rays is then provided by the isotropic source population (also observed by PAO). The reason why this scenario can still provide an acceptable fit is that the TA composition observables are not well constrained at these very high energies. However, we must also note that the fit quality provided by an extreme accelerator is overall worse compared to our baseline model, as we can see by the values of χ^2/d.o.f. listed in Tab. 4

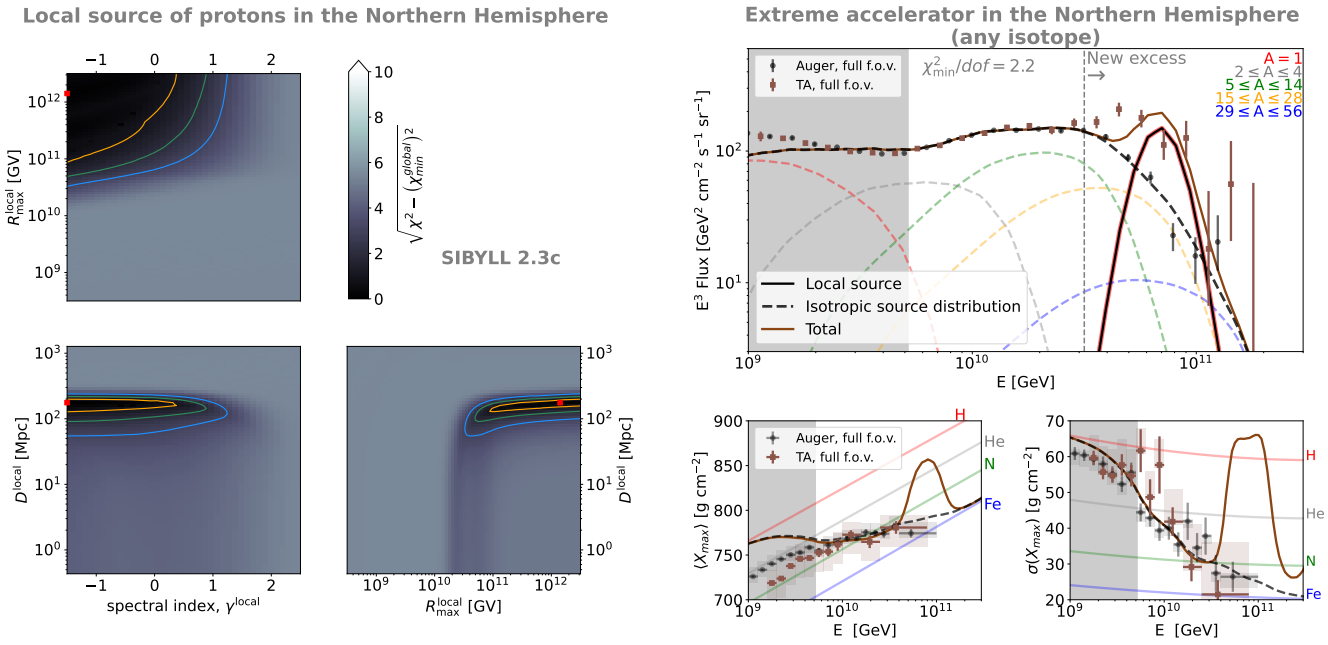

Figure 9. *Left:* Parameter space for a local source for a joint fit to PAO and TA data when considering an isotropic source distribution and a local source in the Northern Hemisphere that emits a pure protons composition. *Right:* Spectra (upper panels) and composition observables (lower panels) predicted by the models corresponding to the best-fit case for an extreme accelerator scenario.

Table 4. Best-fit parameter values obtained from a joint fit to PAO and TA data, for the case of an extreme local accelerator in the ZeV regime. We show the results for different emitted mass groups, considering Sybill as the air shower model, and assuming an energy-independent systematic shift in the experiment energy scales. The best-fit values of the systematic shifts are the same for all isotopes, as listed in Tab. 1. We note that the parameters for silicon are depicted as red squares in the right panel of Fig. 3 (baseline model), and the case of protons is shown in the left panel of Fig. 9.

	H	He	N	Si	Fe
SIBYLL 2.3C					
$\gamma^{\rm local}$	< 0.3	< 0.0	< 0.0	< 0.4	< 0.1
$R^{\rm local}_{\rm max}$ (GV)	$> 1.0 \times 10^{11}$	$> 3.0 \times 10^{11}$	$> 2.2 \times 10^{11}$	$> 1.8 \times 10^{11}$	$> 1.6 \times 10^{11}$
$L^{\rm local}_{\rm CR}$ (erg s^{-1})	$7.6^{+14.7}_{-7.4} \times 10^{45}$	$1.8^{+0.4}_{-1.7} \times 10^{45}$	$1.3^{+0.3}_{-1.3} \times 10^{45}$	$3.5^{+1.4}_{-3.2} \times 10^{45}$	$1.7^{+0.7}_{-1.2} \times 10^{44}$
$D^{\rm local}$ (Mpc)	$176.2^{+18.7}_{-46.1}$	$176.2^{+18.7}_{-46.1}$	$176.2^{+18.7}_{-46.1}$	$13.9^{+9.2}_{-13.4}$	$95.9^{+99.0}_{-43.8}$
χ^2 / d.o.f.	88.3 / 40	88.3 / 40	88.3 / 40	88.3 / 40	88.3 / 40
EPOS-LHC					
$\gamma^{\rm local}$	< 0.5	< 0.2	< 0.2	< 0.4	< 1.3
$R^{\rm local}_{\rm max}$ (GV)	$> 8.0 \times 10^{10}$	$> 1.8 \times 10^{10}$	$> 1.9 \times 10^{10}$	$> 1.8 \times 10^{10}$	$> 1.6 \times 10^{10}$
$L^{\rm local}_{\rm CR}$ (erg s^{-1})	$6.7^{+19.8}_{-6.4} \times 10^{45}$	$9.1^{+17.9}_{-8.8} \times 10^{45}$	$8.1^{+12.1}_{-7.7} \times 10^{45}$	$3.4^{+2.4}_{-2.1} \times 10^{45}$	$1.5^{+1.5}_{-0.9} \times 10^{44}$
$D^{\rm local}$ (Mpc)	$176.2^{+18.7}_{-32.3}$	$176.2^{+18.7}_{-46.1}$	$176.2^{+18.7}_{-46.1}$	$176.2^{+18.7}_{-46.1}$	$176.2^{+18.7}_{-32.3}$
χ^2 / d.o.f.	100.3 / 40	100.4 / 40	100.3 / 40	100.3 / 40	100.2 / 40
QGSJET-II-04					
$\gamma^{\rm local}$	< 0.6	< 0.3	< 0.2	< 0.4	< 1.4
$R^{\rm local}_{\rm max}$ (GV)	$> 8.0 \times 10^{10}$	$> 1.6 \times 10^{11}$	$> 1.8 \times 10^{10}$	$> 1.6 \times 10^{10}$	$> 1.4 \times 10^{10}$
$L^{\rm local}_{\rm CR}$ (erg s^{-1})	$2.7^{+0.6}_{-2.1} \times 10^{46}$	$1.3^{+1.4}_{-0.8} \times 10^{45}$	$9.4^{+11.1}_{-4.5} \times 10^{35}$	$3.4^{+2.5}_{-0.6} \times 10^{45}$	$7.8^{+9.7}_{-1.9} \times 10^{43}$
$D^{\rm local}$ (Mpc)	$194.9^{+10.2}_{-51.0}$	$176.2^{+18.7}_{-46.1}$	$176.2^{+18.7}_{-46.1}$	$176.2^{+18.7}_{-46.1}$	$176.2^{+18.7}_{-46.1}$
χ^2 / d.o.f.	252.8/ 40	252.9 / 40	252.8 / 40	252.8 / 40	252.8 / 40

D. FITTING TA DATA WITH AN ISOTROPIC SOURCE POPULATION

For the sake of comparison, we now evaluate how well a purely isotropic source population can describe the TA data set above 5 EeV (i.e. neglecting now PAO measurements). The best-fit parameters of the isotropic source population are marked with brown squares in the left panel of Fig. 10. For comparison, we show as red dots the best-fit parameters obtained by Heinze et al. (2019) when fitting only PAO data. On the right-hand panel, we show the predicted observables for our TA-only fit. The respective parameter values are listed in Tab. 5.

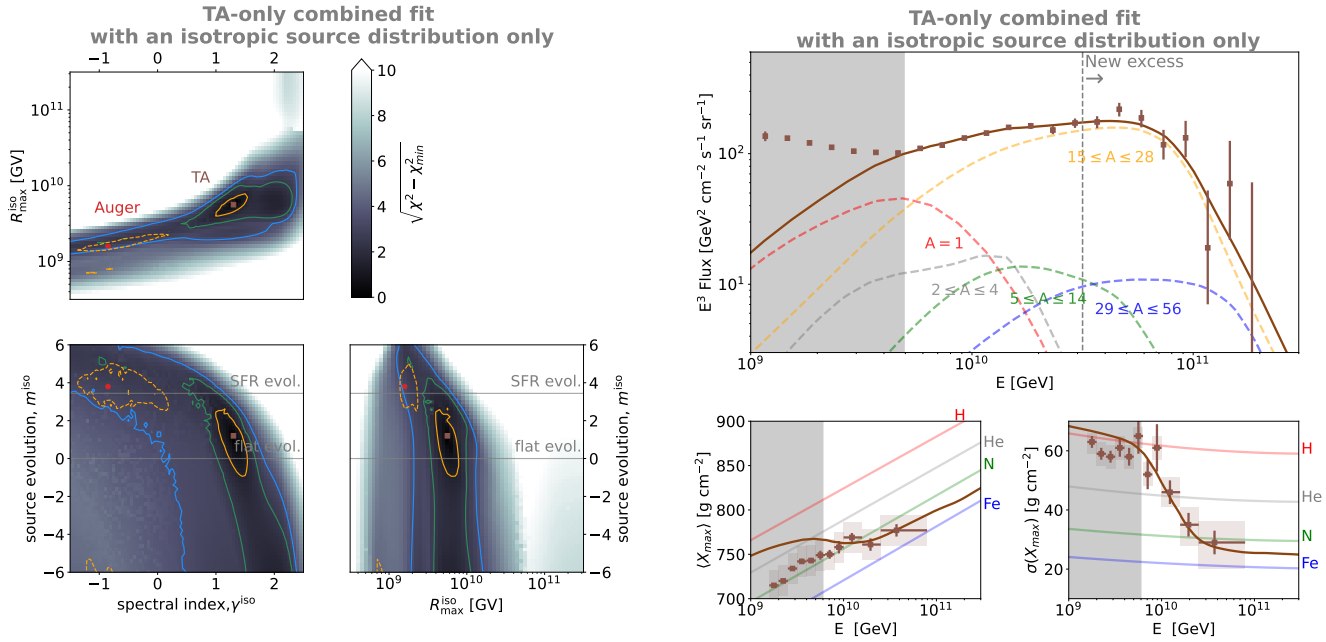

Figure 10. *Left:* Parameter space of a purely isotropic source distribution, based on a fit to the TA spectrum and composition data. The best-fit parameters, listed in Tab. 5, are shown as a brown dot, and for comparison we show as a red dot the best-fit to PAO data (Heinze et al. 2019). The solid yellow, green and blue contours correspond to the 1-, 2- and 3σ regions of our TA-only fit, while the dash yellow line is the 1σ region of the PAO-only fit. A direct comparison is not possible because of the different values of $\chi^2_{\rm min}$ and numbers of d.o.f. for the two combined fits. *Right:* Spectra (upper panels) and composition observables (lower panels) corresponding to the best-fit parameters of our TA-only fit.

As we can see, TA data can be fitted with an isotropic source population with a value of $\chi^2/\text{d.o.f.} = 22.9/15 = 1.5$, in the case where Sibyll is considered, while for the other two air shower models that value is higher, as listed in Tab. 5.

These results are similar to the second-best minimum obtained by Bergman (2019), who considered EPOS-LHC and QGSJET-II-04 as air shower models. We do not obtain the same best-fit minimum obtained by Bergman (2019) because of differences in the analysis method: firstly, we consider $m^{\rm iso}$ as a free parameter, while Bergman (2019) fixed its value to $m^{\rm iso}= 3$. Secondly, in that work the authors used the $X_{\rm max}$ distributions, while we based ourselves only on the mean and variance values of the $X_{\rm max}$ distribution, which are the only publicly available data. More information would be necessary for a more detailed analysis of the differences between these two results.

Table 5. Best-fit parameters obtained from the fit to the TA spectrum and composition data, assuming only an isotropic source distribution. The results are shown for the three different air shower models tested. The case where Sibyll was considered is shown in Fig. 10.

	Sibyll 2.3c	EPOS-LHC	QGSJET-II-04
$\gamma^{\rm iso}$	$1.40^{+0.10}_{-0.15}$	$1.40^{+0.15}_{-0.10}$	$0.10^{+0.15}_{-0.30}$
$R^{\rm iso}_{\rm max}$ (GV)	$7.1^{+0.9}_{-1.5} \times 10^9$	$7.9^{+2.1}_{-0.9} \times 10^9$	$3.2^{+0.3}_{-0.3} \times 10^9$
$m^{\rm iso}$	$-0.8^{+1.0}_{-2.2}$	< -4	< -5.2
$f_A(\%)$			
H	$26.258^{+18.687}_{-12.814}$	$28.512^{+17.681}_{-12.879}$	$50.989^{+25.081}_{-25.589}$
He	$0.034^{+99.956}_{-0.034}$	$0.010^{+99.965}_{-0.010}$	$36.110^{+10.885}_{-9.623}$
N	$0.006^{+99.936}_{-0.006}$	$30.493^{+9.236}_{-7.894}$	$12.625^{+0.526}_{-0.508}$
Si	$72.023^{+1.737}_{-1.805}$	$40.357^{+6.428}_{-6.113}$	$0.000^{+82.967}_{-0.000}$
Fe	$1.680^{+5.901}_{-1.325}$	$0.628^{+21.744}_{-0.614}$	$0.277^{+0.023}_{-0.021}$
$\delta_E^{\rm TA}(\%)$	$-17.6^{+3.9}_{-3.4}$	$-14.1^{+5.4}_{-3.9}$	$21.0^{+0.0}_{-1.5}$
$\delta^{\rm TA}_{\langle X_{\rm max}\rangle}(\%)$	0 (fixed)	0 (fixed)	0 (fixed)
$\delta^{\rm TA}_{\sigma(X_{\rm max})}(\%)$	0 (fixed)	0 (fixed)	0 (fixed)
χ^2 / d.o.f.	22.9 / 15	30.2 / 15	50.9 / 15